

1 Upper mantle mush zones beneath low 2 melt flux ocean island volcanoes: 3 insights from Isla Floreana, Galápagos

4 Matthew L. M. Gleeson^{1*}, Sally A. Gibson¹ and Michael J. Stock^{1,2}

5 ¹Department of Earth Sciences, University of Cambridge, Downing Street, CB2 3EQ, UK

6 ²Department of Geology, Trinity College Dublin, College Green, Dublin 2, Ireland.

7 *Corresponding author email address: mlm3@cam.ac.uk

8 **ABSTRACT**

9 The physicochemical characteristics of sub-volcanic magma storage regions have important
10 implications for magma system dynamics and pre-eruptive behaviour. The architecture of magma
11 storage regions located directly above high buoyancy flux mantle plumes (such as Kīlauea, Hawaii
12 and Fernandina, Galápagos) are relatively well understood. However, far fewer constraints exist on
13 the nature of magma storage beneath ocean island volcanoes that are distal to the main zone of mantle
14 upwelling or above low buoyancy flux plumes, despite these systems representing a substantial
15 proportion of global ocean island volcanism. To address this, we present a detailed petrological study
16 of Isla Floreana in the Galápagos Archipelago, which is characterised by an extremely low flux of
17 magma into the lithosphere from the underlying mantle plume. Detailed *in situ* major and trace
18 element analyses of crystal phases within exhumed cumulate xenoliths, lavas and scoria deposits,
19 indicate that magma storage beneath Floreana is dominated by crystal-rich domains (i.e. mush). Trace
20 element disequilibria between cumulus phases and erupted melts, as well as trace element zoning
21 within the xenolithic clinopyroxenes, reveals that reactive porous flow (previously identified beneath
22 mid-ocean ridges) is an important process of melt transport within these crystal-rich storage regions.
23 In addition, application of three petrological barometers reveal that the Floreana mush zones are
24 located in the upper mantle, at a depth of 23.7 ± 5.1 km. Our barometric results are compared to recent
25 studies of high melt flux volcanoes in the western Galápagos, Hawaii and Iceland, and demonstrate
26 that the flux of magma from the underlying mantle source represents a first-order control on the depth
27 and physical characteristics of magma storage beneath ocean island volcanoes.

28 **KEY WORDS**

29 Galápagos; magma storage; reactive porous flow; barometry.

30 **1 INTRODUCTION**

31 The physicochemical characteristics (such as size, pressure, volatile content and geochemical
32 heterogeneity) of magma storage at volcanic centres located directly above high buoyancy flux mantle
33 plumes (e.g. Kīlauea, Hawaii and Isabela, Galápagos) have been subject to intense study over the past
34 few decades (Bagnardi et al., 2013; Clague and Denlinger, 1994; Geist et al., 1998; Naumann and
35 Geist, 1999; Park et al., 2007; Pietruszka et al., 2015; Poland et al., 2015; Stock et al., 2018; Wieser et
36 al., 2020, 2019). Systems such as Kīlauea are characterised by frequent volcanic activity, and
37 geophysical (seismicity, ground deformation) and geochemical (gas emissions) monitoring is
38 prevalent. Monitoring data, combined with petrological and geochemical analysis of erupted products
39 (mineral textures, deformation characteristics and chemistry) provide important insights into the
40 architecture and dynamics of their sub-volcanic plumbing systems (Amelung et al., 2000; Davidge et
41 al., 2017; Geist et al., 2014; Hartley et al., 2018; Kilbride et al., 2016). However, these systems
42 (which we term ‘high melt flux’) represent only one endmember of global plume-derived volcanism.
43 Low melt flux systems, either above low buoyancy flux plumes (e.g. Canary Islands; Longpre et al.,
44 2014) or at volcanic systems distal to the centre of mantle melting at high buoyancy flux mantle
45 plumes (e.g. eastern and southern Galápagos; Harpp and Geist, 2018), are the other endmember.

46 Although a substantial number of Holocene hotspot-related volcanic systems are located in regions
47 characterised by a relatively low flux of magma into the lithosphere (e.g. Samoa, Canary Islands,
48 Cape Verde; Global Volcanism Program, 2013), only a small number of eruptions have been observed
49 (and recorded) at these systems since the advent of modern volcano monitoring techniques. As a
50 result, few constraints exist on the conditions of magma storage in regions characterised by a low flux
51 of magma into the lithosphere, relative to volcanic centres located above the centre of mantle plumes
52 with a large buoyancy flux (and thus generating a large flux of magma). The flux of mantle-derived
53 magma into the lithosphere is important because it is thought to impart a first-order control on the
54 development of large silicic magma bodies (Barker et al., 2020) and the homogeneity of erupted

55 liquids (Geist et al., 2014). Furthermore, placing constraints on the physicochemical characteristics of
56 magma storage at low melt flux ocean island volcanoes is essential for determining the influence of
57 mantle dynamics and melt generation processes on the structure and physical characteristics of sub-
58 volcanic magma plumbing systems. In the absence of detailed monitoring data, petrological and
59 geochemical analyses of volcanic products from past eruptions represent the only available tools for
60 determining the structure and processes operating within these systems.

61 Isla Floreana in the south-eastern Galápagos Archipelago is currently located ~100 km downstream
62 from where the Galápagos plume impacts on the base of the lithosphere beneath the island of Isabela
63 in the western archipelago (Fig. 1; Villagómez et al., 2014). Hence, although the Galápagos plume has
64 a relatively high buoyancy flux (compared to regions such as the Canary Islands; Jackson et al.,
65 2017), Floreana's location relative to the main zone of mantle plume upwelling results in an
66 extremely low flux of magma entering the lithosphere and, consequently, very infrequent volcanic
67 activity (Harpp et al., 2014a; Harpp and Geist, 2018). In this paper, we present a thorough petrological
68 study of scoria, lava and xenolith samples from Floreana and place constraints of the structure, depth
69 and crystallinity of magmatic systems beneath this low melt flux ocean island volcano. We compare
70 our results with more frequently active volcanic centres in the western Galápagos (near the centre of
71 plume upwelling; Geist et al., 1998; Naumann and Geist, 1999; Stock et al., 2018), as well as Iceland
72 and Hawaii (Hammer et al., 2016; Hartley et al., 2018; Poland et al., 2015), to investigate how the
73 flux of magma into the lithosphere influences the depth and crystallinity of sub-volcanic magma
74 storage regions.

75 **2 GEOLOGICAL BACKGROUND**

76 The Galápagos Archipelago in the eastern equatorial Pacific is one of the most volcanically active
77 regions on Earth, with eruptions typically occurring every 2–3 years (Global Volcanism Program,
78 2013). Although most historic Galápagos eruptions have taken place on the two westernmost islands
79 of Isabela and Fernandina (Fig. 1), infrequent volcanic activity has also occurred on several islands in

80 the eastern and southern Galápagos (e.g. Santiago in 1906 and Marchena in 1991; Global Volcanism
81 Program, 2013).

82 Volcanoes in the western Galápagos likely emerged within the last 500 kyr (Naumann and Geist,
83 2000), whereas those in the eastern and south-eastern Galápagos are considerably older (eruption ages
84 up to 2.3 Ma and 3.2 Ma have been measured on San Cristobal and Espanola, respectively; Bailey,
85 1976; Geist et al., 1986). In addition, substantial differences in geomorphology and the style of
86 volcanic activity are observed across the archipelago (Geist et al., 1995; Harpp et al., 2014a; Harpp
87 and Geist, 2018). For example, volcanoes in the western archipelago are typified by large summit
88 calderas (<700m deep), which are not present on the eastern islands (Chadwick and Howard, 1991;
89 Cleary et al., 2020; Harpp and Geist, 2018).

90 Geochemical distinctions between the western and eastern/southern Galápagos islands are also
91 observed, which are primarily related to variations in the composition of the underlying mantle source
92 (Geist et al., 1988; Gibson and Geist, 2010; Gleeson et al., 2020; Harpp and White, 2001; White et al.,
93 1993) or the volume flux of mantle-derived magma that ascends into the lithosphere (Geist et al.,
94 1995, 2014; Gibson et al., 2016; Harpp and Geist, 2018). For example, variations in the flux of mantle
95 derived magma are hypothesised to influence the geochemical heterogeneity of erupted basalts at each
96 island: volcanoes in the western archipelago typically erupt a very narrow range of basaltic
97 compositions over hundreds of millennia during their main shield building phase, whereas basalts
98 erupted from a single island in the eastern and/or south-eastern archipelago, such as Floreana, tend to
99 display far greater compositional heterogeneity (Geist et al., 2014; Harpp and Geist, 2018).

100 Floreana is characterised by numerous scoria cones (up to ~600m elevation at Cerro Pajas) and
101 blocky, heavily vegetated lava flows that can typically be traced to the cone from which they
102 originated (Harpp et al., 2014a). The crustal thickness beneath Floreana is ~16 km, similar to that
103 observed in the western Galápagos 10–18 km (Feighner and Richards, 1994), and the lithospheric
104 thickness beneath the western and south-eastern Galápagos is very similar (~50–60 km; Gibson and
105 Geist, 2010). However, recent work has shown that the volumetric eruption rate on Floreana is 1–10
106 m³·yr⁻¹ over the past 1–1.5 Myrs, millions of times lower than the current effusion rate at volcanoes in

107 the western Galápagos (cf. $\sim 4.4 \cdot 10^6 \text{ m}^3 \cdot \text{yr}^{-1}$ at Fernandina; Harpp et al., 2014a; Kurz et al., 2014).
108 This variation in volumetric eruption rate likely reflects a substantially lower flux of magma into the
109 lithosphere beneath Floreana than beneath each volcanic centre in the western Galápagos.
110 Additionally, Floreana has a high proportion of pyroclastic deposits compared to the other Galápagos
111 islands (Harpp et al., 2014a) and eruption deposits typically contain a large number of cumulate
112 xenoliths (Lyons et al., 2007). The abundance of pyroclastic deposits and xenoliths on Floreana has
113 been interpreted as evidence for very high magma ascent rates (Harpp et al., 2014a).
114 Floreana is one of the only Galápagos islands that displays evidence for multiple stages in its volcanic
115 evolution. Submarine parts of the island have isotopic and trace element characteristics that are
116 similar to recent basalts erupted on southern Isabela (e.g. Sierra Negra and Cerro Azul, Fig. 1A),
117 whereas the subaerial material is isotopically distinct (high $^{206}\text{Pb}/^{204}\text{Pb}$ ratios; Harpp et al., 2014). The
118 trace element and isotopic variation in the erupted basalts is mirrored in xenoliths found in the
119 Floreana lava and scoria deposits: gabbroic xenoliths have radiogenic isotope ratios that are similar to
120 modern Isabela basalts, whereas wehrlitic xenoliths have trace element and isotopic compositions that
121 resemble recent Floreana subaerial basalts (Lyons et al., 2007). Variations in the isotopic
122 characteristics of the Floreana lavas (submarine vs subaerial) and xenoliths (gabbros vs wehrlites) are
123 thought to indicate a change in the mean composition of magma produced by mantle melting beneath
124 the island at $\sim 1\text{--}1.5 \text{ Ma}$ (Harpp et al., 2014a). In this study, we focus on constraining the depth and
125 physical characteristics of magma storage during the most recent period of volcanic activity on Isla
126 Floreana ($< 1\text{--}1.5 \text{ Ma}$) using chemical and textural analysis of crystal phases in lava flows and
127 xenolithic nodules.

128 **3 SAMPLES AND PETROGRAPHY**

129 The Floreana samples analysed in this study were collected during a field campaign to the northern
130 part of the island in June 2017 and consist of lavas (27 samples), scoria (2 samples) and xenoliths (4
131 wehrlite, 3 dunite and 2 gabbro samples; Fig. 1B). Most lava samples were collected from the
132 unaltered, low vesicularity cores of blocky flows or glassy flow fronts. The scoria samples were

133 collected from two separate deposits and comprise rapidly cooled tephra fragments (~0.5–2 cm
134 across; 17MMSG16) and scoria bombs (~10 cm across; 17MMSG20). Xenolithic fragments (3–15cm
135 across) were sampled from two different scoria cones on the north-east coast of Floreana and are also
136 found within most lava flows across the entire island (Fig. 1).

137 **3.1 Lavas and scoria**

138 The lava and scoria samples analysed in this study are typically olivine phyric with minor andehral
139 clinopyroxene and very rare orthopyroxene. Except for small plagioclase laths in the microcrystalline
140 groundmass, plagioclase crystals are extremely rare in Floreana lavas. Plagioclase macrocrysts are
141 only present in one of our lava samples (17MMSG29) where they occur as isolated phenocrysts and in
142 plagioclase-olivine crystal clots (Table S.1). Abundant olivine and the absence of plagioclase in the
143 Floreana lavas and scoria contrasts with basalts in the central, northern, and western parts of the
144 Galápagos Archipelago, where plagioclase-phyric and ultraphyric basalts are common (Geist et al.,
145 2002; Gibson et al., 2012; Harpp et al., 2014b).

146 Despite their relatively simple mineralogy, Floreana lava and scoria samples contain texturally diverse
147 olivine crystals which can be divided into five distinct groups (Fig. 2):

- 148 - Group 1 olivines are present in all lava and scoria samples and are the most abundant type of
149 olivine found in the Floreana basalts (~60-70% of all crystals). They are characterised by
150 homogeneous cores and narrow normally zoned rims (Fig. 2A). Group 1 olivines are
151 generally subhedral to euhedral.
- 152 - Group 2 olivines are the second most abundant group in the Floreana lava and scoria deposits
153 (~20-30%) and display reverse zoning patterns. They are typically euhedral, with occasional
154 small embayments (Fig. 2B).
- 155 - Group 3 olivines are also reversely zoned, but are distinguished by skeletal overgrowths,
156 indicating significant undercooling of the host magma and rapid crystal growth (Fig. 2C;
157 Donaldson, 1976; Welsch et al., 2014). Group 3 olivines are less abundant than Groups 1 and
158 2 olivines in Floreana lava and scoria deposits (<10%).

- 159 - Group 4 olivines are present in low abundance in the Floreana lava and scoria deposits
160 (<10%). They have homogeneous cores and reverse-zoned rims (up to ~300 μm thick). The
161 rims have sieve textures, indicating resorption and chemical disequilibrium with their carrier
162 melts (Fig. 2D).
- 163 - Group 5 olivines are only found in a minority of samples and are characterised by the
164 presence of 4 compositional zones with alternating high and low forsterite contents (visible in
165 back-scattered electron images; Fig. 2E and F).

166 3.2 Xenoliths

167 3.2.1 Gabbroic xenoliths

168 Floreana gabbroic xenoliths predominantly comprise plagioclase (33–66 vol.%), clinopyroxene (28–
169 46 vol.%) and orthopyroxene (5–15 vol.%), with little or no olivine (Table S.2). Plagioclase and
170 pyroxene crystals are typically >500 μm and grain sizes are relatively constant within a single
171 xenolith sample. Where three plagioclase grains meet at a triple junction, 120° grain boundaries
172 indicate a high degree of textural equilibrium (Fig. 3A; Holness et al., 2005). Some of the gabbros
173 display clear clinopyroxene-rich and plagioclase-rich layers (2–5 mm), whereas others have a more
174 irregular mineral distribution.

175 3.2.2 Dunitic xenoliths

176 Cumulus olivine dominates dunitic Floreana xenoliths (>90 vol.%). The olivine crystals are subhedral
177 to euhedral and may have undergone partial textural re-equilibration, with some olivine triple
178 junctions approaching 120° grain boundaries. Minor intercumulus clinopyroxene is present along
179 grain boundaries and between pre-existing olivine crystals (Fig. 3B).

180 3.2.3 Wehrlitic xenoliths

181 Floreana wehrlitic xenoliths contain olivine (>50 vol.%), clinopyroxene (20–40 vol.%),
182 orthopyroxene (~0–7 vol.%) and minor spinel (<1 vol.%; Table S.1). Clinopyroxene typically occurs
183 as large (<5 mm) oikocrysts, which enclose rounded olivine chadacrysts (<500 μm in diameter and
184 separated by distances of <400 μm ; Fig. 2C and D). In the most pyroxene-rich samples (e.g.
185 17MMSG03a), clinopyroxene crystals contain fine-scale orthopyroxene exsolution lamellae (Fig. 2E

186 and F). Olivine grains that are not enclosed by clinopyroxene are typically larger (>1 mm) and more
187 euhedral than the chadacrysts. In some samples, the boundary between clinopyroxene and olivine
188 crystals is characterised by a thin (<20-30 μm) layer of glass and very fine-grained microcrysts.
189 Orthopyroxene is an intercumulus phase in the wehrlitic xenoliths and has an anhedral morphology,
190 infilling the space between earlier formed clinopyroxene and olivine grains. Our observations of
191 dunitic and wehrlitic xenoliths (which have the isotopic signatures of modern day Floreana basalts;
192 Lyons et al., 2007) indicate that the typical order of crystallisation beneath Floreana is olivine,
193 followed by clinopyroxene, with little to no crystallisation of plagioclase.

194 **4 ANALYTICAL METHODOLOGY**

195 **4.1 Electron microprobe analysis**

196 Glass chips, olivine and clinopyroxene crystals were hand-picked from crushed scoria and lava
197 samples, mounted in epoxy or indium, and then ground and polished prior to analysis (crystals
198 mounted in indium were polished individually prior to mounting). Xenolithic crystals were analysed
199 as individual crystals mounted in indium or *in situ* in petrographic thin sections. The major and minor
200 element concentrations of olivine, clinopyroxene and glass were measured using a Cameca SX100
201 electron microprobe in the Department of Earth Sciences, University of Cambridge. Calibrations were
202 made using mineral and metal standards prior to each analytical session (see Gleeson and Gibson,
203 2019 for details). Glasses in the two Floreana scoria samples were analysed using a 6 nA, 15 kV,
204 defocused (5 μm) beam for most elements. Na and K were analysed first (10 s peak count time) to
205 avoid alkali migration. Other elements were analysed with peak count times of 10 s (Si), 20 s (Fe), 30
206 s (Al, P, Ca, Mg), 40 s (Mn), or 60 s (Ti). Sulphur was analysed last using a 20 nA beam current and a
207 60 s peak count time.

208 Pyroxene compositions were determined by spot analyses using a 20 nA, 15 kV, focused ($\sim 1 \mu\text{m}$)
209 beam, with Na, K and Si analysed first (10 s). Element maps of Cr, Ti, and Al in key clinopyroxene
210 crystals from the Floreana xenoliths were created using a 60 nA, 15 kV, focused ($\sim 1 \mu\text{m}$) beam, with
211 a dwell time of 150 ms. Cr counts were collected on a PET and a LIF crystal, Al counts were

212 collected on two TAP crystals, and Ti counts were collected on a PET crystal. Olivine electron
213 microprobe analysis was carried out using the method outlined in Gleeson and Gibson (2019).
214 Analytical uncertainties were tracked through analysis of appropriate Smithsonian Microbeam
215 Standards (Jarosewich et al., 1980). Accuracy is typically between 98 and 102% for all phases. 2σ
216 analytical precision of clinopyroxene and olivine analysis is typically better than 2–3% for major
217 elements (>1 wt%) and typically ~5-10% for minor elements (<1 wt%). Similarly, the 2σ precision for
218 glass analysis is typically <3% for major elements, ~5% for Na, and ~10% for K (See Supplementary
219 File).

220 **4.2 Laser ablation Inductively Coupled Plasma Mass Spectrometry**

221 Trace element concentrations were measured in the apparent cores (i.e. as exposed in the 2D plane) of
222 clinopyroxene crystals from scoria and xenolith samples using an ESI193 laser coupled to a Nexion
223 350D inductively coupled plasma mass spectrometer in the Department of Earth Sciences, University
224 of Cambridge. Analyses were collected in spot mode using a 20 Hz laser repetition rate, 4 J/cm²
225 fluence and 80 μ m spot size, or in transect mode using a 10 Hz repetition rate, 3.5 J/cm² fluence and
226 30 μ m spot size. For transects, individual spots were offset into two (alternating) lines to increase the
227 spatial resolution. Laser ablation inductively coupled plasma mass spectrometry (LA-ICP-MS) data
228 reduction was carried out in Iolite[®], with NIST 612SRM as the standard reference material and Ca
229 (from electron microprobe analysis) as the internal reference standard. Analytical accuracy was
230 tracked using a USGS glass standard (Jochum et al., 2016) and is between 95% and 105% for most
231 elements (See Supplementary File). 2σ analytical precision of spot analyses was monitored through
232 analysis of an in-house clinopyroxene standard and is 5–10% for the light rare-earth elements
233 (LREE), Y, Sr, and Zr and 10–20% for the heavy rare earth element (HREE). 2σ analytical precision
234 is ~10% for all elements of interest (Ce, Y) in transect analyses.

235 **5 GLASS AND MINERAL CHEMISTRY**

236 **5.1 Matrix glass compositions**

237 The matrix glass compositions measured in one scoria (17MMSG16) and one glassy lava sample
238 (17MMSG12) from Floreana have very similar MgO concentrations (6.06–6.36 wt%) but exhibit
239 differences in the concentrations of other elements (Fig. 4). For example, sample 17MMSG12 has
240 consistently lower TiO₂ and Al₂O₃ concentrations than 17MMSG16, which must either reflect
241 heterogeneity in the composition of primary mantle melts or variations in crustal processing (e.g. the
242 extent of plagioclase or clinopyroxene crystallisation; Fig. 4). Differences between our matrix glass
243 major element analyses and previously-published whole-rock data from Floreana (Harpp et al., 2014a)
244 are primarily due to olivine accumulation in the whole-rock samples (additional accumulation of
245 clinopyroxene may explain the high CaO content of some whole-rock samples; Fig. 4C).

246 Our Floreana matrix glass analyses have higher Al₂O₃ concentrations than basaltic glass and whole-
247 rock measurements from the western Galápagos Archipelago (excluding whole-rock samples with
248 accumulated plagioclase, Fig. 4D; Geist et al., 2002). This indicates substantially lower extents of
249 plagioclase fractionation in the Floreana magmatic system and is consistent with the scarcity of
250 plagioclase phenocrysts in erupted Floreana lavas. Reduced plagioclase crystallisation could be due to
251 the major element composition or H₂O content of primary mantle melts and/or the increased pressure
252 of magma storage (Asimow and Langmuir, 2003; Neave et al., 2019; Thompson, 1987; Winpenny and
253 MacLennan, 2011).

254 **5.2 Olivine compositions**

255 Olivine crystals in our Floreana lava and scoria samples show large variations in their forsterite
256 contents (Fo = 70–92, where Fo=(Mg/(Mg+Fe²⁺) molar) with histograms showing a primary density
257 peak at Fo~85 (Fig. 5), more primitive than the olivine composition in equilibrium with basaltic
258 glasses from Floreana (K_D = 0.30; Roeder and Emslie, 1970). Although there is no clear correlation
259 between Fo and Ca concentration in these crystals, the most forsteritic olivines (Fo>83) have

260 extremely diverse Ca contents (~250 to ~2600 ppm; Fig. 5), whereas crystals with lower Fo contents
261 (<83) have ubiquitously low Ca concentrations (<1500 ppm). Floreana olivines separated from the
262 lava and scoria samples also have a large range of Ni concentrations (~700 to ~3200 ppm), consistent
263 with crystallisation from a peridotite-derived melt (Fig. 5; Gleeson and Gibson, 2019; Herzberg,
264 2011; Matzen et al., 2017b, 2017a). All olivine crystals analysed in the wehrlite and dunite xenoliths
265 have a narrow range of Fo contents (83-87) and, crucially, have uniformly low Ca concentrations
266 (<1000 ppm) and moderately high Ni contents (~2000 ppm). The range in Ca contents contrasts with
267 olivines from other Galápagos islands where Ca is typically >1000 ppm (Gleeson and Gibson, 2019;
268 Vidito et al., 2013). The Ca and Ni contents of our Floreana olivines are inversely related at a set Fo
269 content (Fig. 5).

270 **5.3 Clinopyroxene compositions**

271 *5.3.1 Major elements*

272 The Floreana clinopyroxenes analysed in this study (from scoria and xenolith samples) are augites
273 ($\text{En}_{48.5}\text{Fs}_{31.5}\text{Wo}_{19.5}$) and have a relatively high Mg# (0.85–0.90; $\text{Mg\#} = \text{Mg}/(\text{Mg}+\text{Fe}_t)$ molar). The
274 clinopyroxenes typically contain very high Na concentrations (<1.58 wt% Na_2O , <0.11 Na atoms per
275 formula unit; Fig. 6A) and, correspondingly, up to 10% of the jadeite component. In general,
276 clinopyroxene separates from scoria samples display a wide range of Na concentrations, whereas the
277 xenolithic clinopyroxenes have high Na contents (Fig. 6A). The Floreana clinopyroxenes display a
278 large range of Cr contents, ranging from <0.05 wt% in the most evolved crystals to ~1.72 wt% in the
279 more primitive crystals (Fig. 6B).

280 *5.3.2 Trace elements*

281 Our Floreana clinopyroxenes display a wide range of geochemical enrichment, with LREE to MREE
282 ratios varying from $[\text{La}/\text{Sm}]_n \sim 0.2$ to $[\text{La}/\text{Sm}]_n \sim 3.1$. Xenolithic clinopyroxenes typically have more
283 enriched trace element ratios (such as $[\text{La}/\text{Sm}]_n$ or $[\text{Ce}/\text{Y}]_n$) than clinopyroxenes from the scoria
284 samples (Fig. 7). Furthermore, the melt $[\text{La}/\text{Sm}]_n$ ratios calculated to be in equilibrium with
285 clinopyroxenes from the scoria and xenolith samples range from ~1 to ~15 (calculated using the

286 elastic strain model of Wood and Blundy (1997) at 1225°C and 700 MPa; Fig. 7B), significantly
287 greater than the range measured in Floreana whole-rock samples (~2–5, with a small number of
288 outliers up to ~7.5; Harpp et al. 2014a). Almost all of the xenolithic crystals, and a large proportion of
289 the clinopyroxenes separated from scoria deposits, are too enriched to be in equilibrium with the
290 typical composition of melts erupted on Floreana (Harpp et al., 2014a). In addition, there is a strong
291 correlation between the Na concentrations and highly/moderately incompatible trace element ratios of
292 the Floreana clinopyroxenes, such that crystal with high incompatible trace element concentrations
293 typically contain a high jadeite component (Fig. 7A).

294 **6 MAGMA SYSTEM ARCHITECTURE BENEATH** 295 **ISLA FLOREANA**

296 **6.1 Mush crystallisation and textural equilibration**

297 Based on pyroxene trace element and radiogenic isotope ratios, Lyons et al. (2007) hypothesised that
298 gabbroic xenoliths in the Floreana lava and scoria deposits formed in an ancient (>1-1.5 Ma)
299 magmatic system, compositionally similar to those currently beneath Cerro Azul and Sierra Negra
300 volcanoes in the western Galápagos Archipelago. In contrast, wehrlite xenoliths preserve isotopic
301 ratios similar to more recent subaerial lavas on Floreana, suggesting that they are fragments of the
302 present-day magmatic system (Lyons et al., 2007).

303 Our wehrlitic xenoliths preserve an original igneous texture (clinopyroxene oikocrysts surrounding
304 olivine chadacrysts; Wager et al., 1960) and display no evidence of textural re-equilibration (e.g. 120°
305 dihedral angles) or metamorphic breakdown of plagioclase (e.g. pseudomorphs or relict cores; Lyons
306 et al., 2007). The presence of orthopyroxene lamellae in some clinopyroxenes indicates that they
307 cooled relatively slowly (Poldervaart and Hess, 1951). Hence, we suggest that the clinopyroxene
308 crystals in our wehrlitic xenoliths grew within an olivine-dominated cumulate mush (i.e. interstitial
309 growth of clinopyroxene oikocrysts; Wager et al., 1960). The rounded morphology and small size of
310 olivine chadacrysts, relative to olivine crystals that are not enclosed by clinopyroxene oikocrysts (Fig.
311 3D), indicates that clinopyroxene growth may have been at the expense of olivine (e.g. Lissenberg

312 and MacLeod, 2016). If clinopyroxene growth is principally within a crystal-rich (i.e. relatively
313 viscous and immobile) mush zone, this could explain its relatively low abundance in Floreana lava
314 and scoria deposits (<5% of separated crystals).

315 In contrast with the wehrlites, three-grain plagioclase triple junctions in our gabbroic xenoliths have
316 ~120° dihedral angles (Fig. 3A), indicating a high degree of textural equilibration (Holness et al.,
317 2019, 2005). Plagioclase textural equilibrium, along with the two-pyroxene phase assemblage,
318 suggests that the gabbroic xenoliths represent magmatic cumulates which were stored at high
319 temperatures (>900°C) on long timescales (Holness et al., 2006). These petrographic observations are
320 consistent with the gabbroic nodules sampling an ancient magmatic system beneath Floreana (>1 Ma;
321 Lyons et al., 2007).

322 **6.2 Mush disaggregation prior to eruption**

323 *6.2.1 Insights from olivine compositional heterogeneity*

324 Olivine crystals separated from the Floreana lava and scoria samples have a wide range of zoning
325 patterns, morphologies, and compositions (Fig. 2). The five olivine groups identified in the Floreana
326 samples have distinct morphologies and zoning patterns (see Section 2 above), suggesting chemically
327 heterogeneous magma storage (Holness et al., 2019). In particular, the most evolved crystals (Group
328 4; Fo~70–75) are in equilibrium with melts that are more evolved than the Floreana erupted basalts.
329 This is consistent with a recent study which identified highly evolved (rhyolitic) magmas beneath
330 basaltic volcanoes in the western Galápagos Archipelago (Stock et al., *in review*).

331 As Fe-Mg interdiffusion in olivine is geologically fast (Costa et al., 2020), preservation of forsterite
332 zoning in the Floreana olivine crystals suggests that multiple magma batches interacted on relatively
333 short pre-eruptive timescales. In Group 5 olivines, for example, four compositional zones are
334 preserved over ~100-200 µm near the rim (Fig. 2E and F). Whilst we do not have enough Group 5
335 olivine crystals to calculate statistically robust timescales of pre-eruptive magma interactions using
336 diffusion chronometry, complex forsterite zoning over ~100 µm is estimated to last <3 yrs at the
337 approximate temperature of basaltic magma storage (~1225°C; using diffusion coefficients from
338 Chakraborty, 2010). Therefore, we suggest that the range of crystal morphologies and major element

339 compositions displayed by the Floreana olivines in lava and scoria deposits indicates mixing and
340 amalgamation of chemically heterogeneous magma storage regions over relatively short timescales
341 prior to eruption.

342 The minor element chemistry of the olivine crystals allows us to investigate the crystallinity of these
343 chemically diverse magma storage regions. Olivine crystals in our Floreana lava and scoria deposits
344 have an unusually low, and large range of Ca concentrations (~250–2600 ppm compared with ~1500-
345 3000 in the eastern Galápagos; Gleeson and Gibson, 2019; Fig. 5A). The lower end of the range in Ca
346 concentrations measured in the Floreana lava and scoria deposits overlaps with those observed in
347 cumulate xenoliths (wehrlites) and thus are unlikely to represent mantle olivines (Thompson and
348 Gibson, 2000). Previous studies have shown that the Ca concentration of magmatic olivine is sensitive
349 to several parameters, including: (i) the temperature of the system (Adams and Bishop, 1982; Köhler
350 and Brey, 1990; Shejwalkar and Coogan, 2013); (ii) the H₂O content of the co-existing melt phase
351 (Gavrilenko et al., 2016); and (iii) the major element composition of the co-existing melt phase
352 (Herzberg, 2011). However, the diversity of Ca concentrations in our Floreana olivines is too large to
353 be caused by variations in T alone (assuming that the difference between the crystallisation
354 temperature and final storage temperature is <300°C; see Section 6.4). In addition, H₂O contents of ~3
355 wt% would be required to explain the lowest Ca concentrations in the Floreana olivines (according to
356 the hygrometer of Gavrilenko et al., 2016), which is far in excess of that measure in Floreana
357 submarine glasses by Peterson et al. (2017). Hence, Ca variations in Floreana olivines likely result
358 from compositional variability in the co-existing melt phase.

359 Although olivine Ca variations are often interpreted to reflect lithological heterogeneity of the mantle
360 source (resulting in primary melt compositional variability), this is inconsistent with the Ni contents
361 of olivine crystals from Floreana (Fig. 5B; Gleeson and Gibson, 2019). An alternative process is
362 therefore required to explain the variability of olivine Ca concentrations and, specifically, the
363 presence of olivine crystals with <1000 ppm Ca. This process must reduce the Ca concentration of the
364 melt phase (and co-existing olivines), without simultaneously reducing the melt Mg# (as low Ca

365 concentrations are observed across the entire range of forsterite contents in the Floreana olivines; Fig.
366 5A) and may be accompanied by slight variations in T or melt H_2O concentration.

367 Evidence for the origin of the low-Ca olivines in the lava and scoria deposits is present in texture and
368 composition of the wehrlitic xenoliths, which contain uniformly low-Ca olivine crystals (<1000 ppm;
369 Fig. 5A). The petrography of the wehrlitic xenoliths attests to clinopyroxene growth within olivine-
370 dominated mush regions. Clinopyroxene crystallisation within this mush would extract CaO and MgO
371 from the residual melt. However, in an olivine-rich mush, the large reservoir of MgO contained within
372 the cumulus olivine grains would buffer the residual melt at a near-constant Mg# during
373 clinopyroxene crystallisation (Meyer et al., 1989). In contrast, the CaO concentration of the melt is
374 not buffered and decreasing melt CaO contents, due to clinopyroxene crystallisation, will cause the
375 CaO concentration of cumulus olivine grains to decrease (as a result of diffusive re-equilibration).
376 Intercumulus clinopyroxene growth would also increase the H_2O concentration of the residual melt
377 phase, decreasing the partition coefficient of Ca into olivine (Gavrilenko et al., 2016). Therefore, if
378 these mush-zone crystals are entrained into ascending melts prior to eruption, growth of
379 clinopyroxene within an olivine-dominated mush could explain the presence of anomalously low Ca
380 concentrations in the Floreana olivines separated from lava and scoria deposits.

381 As the majority of olivine analyses from the Floreana lava and scoria deposits have low Ca
382 concentrations (<1000 ppm) that overlap with those in xenolithic nodules, we suggest that a large
383 proportion of the erupted crystal cargo derives from highly crystalline magma storage regions. Higher
384 Ca concentrations (>1500 ppm) are only found in a small number of forsteritic crystals (Fo>83) in the
385 lava and scoria samples (Fig. 5A). As olivine crystals formed from peridotitic melts that have not
386 undergone clinopyroxene growth will typically have Ca concentrations >1500 ppm (Gleeson and
387 Gibson, 2019; Herzberg, 2011), we interpret these crystals to have grown within liquid-rich magma
388 storage regions where magmatic differentiation occurs by fractional crystallisation.

389 However, olivine crystals from the Floreana lava and scoria deposits cannot simply be divided into
390 low Ca (<1000 ppm) and high Ca (>1500 ppm) populations (Fig. 5A). A substantial number of olivine
391 crystals have intermediate compositions (Ca = 1000–1500). We interpret these as being sourced from

392 regions where growth of clinopyroxene was ongoing at the time of mush disaggregation. Thus, the
393 olivine crystal cargo of the Floreana magmas is predominantly derived from crystal-rich domains that
394 vary from highly crystalline (Ca <1000 ppm) to moderately crystalline (Ca = 1000–1500 ppm). Only
395 a small number of olivine crystals preserve compositions consistent with fractional crystallisation in
396 liquid-rich storage regions (Ca >1500 ppm).

397 6.2.2 *Insights from clinopyroxene major element compositions*

398 The compositions of clinopyroxene crystals from the Floreana scoria also overlap with those in our
399 xenolith samples, supporting the hypothesis that some of the erupted crystals are derived from
400 disaggregated sub-volcanic mush. We used hierarchical cluster analysis to subdivide our 567
401 clinopyroxene major element analyses from the Floreana scoria and xenolith samples to determine the
402 proportion of material that is derived from each xenolith lithology in the erupted crystal cargo. We
403 find that our clinopyroxene analyses form three distinct groups (Fig. 8):

- 404 - Group 1 clinopyroxenes are predominantly from the wehlite and dunite xenoliths and include
405 90% of our analyses from these samples. 39% of clinopyroxenes analysed from the scoria
406 samples also fall into this group.
- 407 - Group 2 clinopyroxenes include all analyses from the gabbroic xenoliths, and ~10% of
408 analyses from crystals separated from the scoria samples.
- 409 - Group 3 clinopyroxenes are dominantly analyses from scoria derived clinopyroxenes (~50%
410 of analyses from the scoria separates). However, 10% of analyses from the wehlite and
411 dunite xenoliths also fall into this group.

412 Of our 248 clinopyroxenes analysed from the Floreana scoria samples, approximately half are
413 classified as Group 3 and thus have major element compositions that do not show any affinity to
414 either the wehlite/dunite or gabbroic cumulates. Therefore, these crystals may represent autocrysts
415 (with growth in liquid-rich magma storage regions). The remainder of clinopyroxene analyses from
416 the scoria samples are either compositionally analogous to those in the wehlite and dunite xenoliths
417 (Group 1; 39%) or the gabbroic xenoliths (Group 2; 11%); we interpret these as representing
418 disaggregated sub-volcanic mush or wall rock. The high proportion of the clinopyroxene crystal cargo

419 that is derived from highly crystalline storage regions beneath Floreana is consistent with our
420 interpretation of olivine minor element concentrations.

421 **6.3 Reactive Porous Flow within a cumulate mush**

422 Whilst the olivine and clinopyroxene major and minor element concentrations show that a large
423 proportion of the erupted crystal cargo is derived from highly crystalline magma storage regions,
424 clinopyroxene trace element concentrations (and zoning) reveal the magmatic processes that operate
425 within these crystal-rich domains. The trace element composition of melts in equilibrium with our
426 clinopyroxene crystals are calculated using the model of Wood and Blundy (1997). The results
427 indicate that many of our clinopyroxene analyses have incompatible trace element ratios (e.g.
428 $[Ce/Y]_n$) which are more enriched than any erupted basalt from Floreana (Harpp et al., 2014a). In fact,
429 nearly all clinopyroxenes analyses from our xenolith samples, and ~50% of clinopyroxene analyses
430 from the scoria samples, record trace element disequilibrium with the typical trace element
431 composition of the Floreana basalts (Fig. 7 and 9). Over-enriched equilibrium melt signatures are
432 characteristics of Group 1 clinopyroxenes (i.e. chemical affinity to the wehrlitic or dunitic xenoliths),
433 whereas crystals that are near trace element equilibrium with Floreana basalts typically have Group 3
434 major element compositions (i.e. the autocrust group).

435 Petrographic observations and olivine minor element data indicate that the Floreana sub-volcanic
436 system is characterised by clinopyroxene crystallisation within an olivine-dominated mush. If the
437 clinopyroxene grew from trapped melt within an olivine-dominated mush, progressive crystallisation
438 would increase the concentration of highly incompatible trace elements (e.g. Ba, La, Ce) relative to
439 less incompatible trace-elements (e.g. Sm, Y) in the residual melt. A simple fractional crystallisation
440 model indicates that ~80% crystallisation is required to generate melt $[Ce/Y]_n$ ratios that are in
441 equilibrium with enriched clinopyroxenes from the scoria samples and even greater extents of
442 crystallisation (~90%) would be required to generate the extremely high $[Ce/Y]_n$ ratios in some of the
443 xenolithic clinopyroxenes (Fig. 9). Such extensive crystallisation would be expected to result in the
444 saturation and crystallisation of plagioclase and other accessory phases (e.g. apatite,

445 magnetite/ilmenite, quartz), which are observed in more evolved xenoliths from Rabida island in the
446 central Galápagos (Holness et al., 2019). However, these phases are absent in the Floreana xenoliths,
447 indicating that another process is responsible for generating the anomalous trace element signatures of
448 the melts in equilibrium with our clinopyroxenes.

449 One possible mechanism for generating the observed trace element over-enrichment is reactive porous
450 flow, where clinopyroxene saturated melts ascend through highly-crystalline magmatic systems
451 causing dissolution of the existing crystal framework and precipitation of clinopyroxene (Lissenberg
452 and MacLeod, 2016). Reactive porous flow can result in net replacement of olivine by clinopyroxene,
453 leading to enrichment of highly- to moderately-incompatible trace elements in the resulting melt and
454 co-existing crystal phases (Coogan et al., 2000; Gao et al., 2007; Lissenberg et al., 2013; Lissenberg
455 and MacLeod, 2016), and is consistent with the petrography of the Floreana xenoliths. For example,
456 major element maps of clinopyroxene crystals in the Floreana wehrlites show that they are zoned,
457 with Ti-rich rims (Fig. 10); equivalent zoning patterns have been attributed to reactive porous flow in
458 plutonic clinopyroxenes from the oceanic crust (e.g. Hess Deep; Lissenberg and MacLeod, 2016).
459 Furthermore, reactive porous flow is consistent with the small size and rounded morphology of
460 olivine chadacrysts. In addition, if pre-existing Cr-spinel was dissolved by the reacting melt, then
461 reactive porous flow could also explain the high Cr contents of clinopyroxene in our wehrlitic
462 xenoliths (Fig. 6; Lissenberg and MacLeod, 2016).

463 To test whether reactive porous flow of clinopyroxene saturated melts through an olivine-dominated
464 mush is consistent with the trace element compositions of melts calculated to be in equilibrium with
465 our Floreana clinopyroxenes, we use the zone refining model of Harris (1957; Fig. 9):

466
$$\frac{C_l}{C_l^o} = \frac{1}{D} - \left(\frac{1}{D} - 1\right)^{-DI}$$

467 (eq. 1)

468 where D is the bulk partition coefficient; C_l^o and C_l are the initial and final concentration of that
469 element in the melt phase, respectively; and I is the 'equivalent volumes of solid processed by the

470 liquid' (Lissenberg and MacLeod, 2016). The model assumes that a migrating melt front depletes solid
471 phases of their incompatible trace elements owing to partial melting, and has previously been
472 employed to investigate geochemical signatures in oceanic gabbros (Lissenberg and MacLeod, 2016).
473 The model produces melts with trace element compositions that are comparable with those in
474 equilibrium with our Floreana clinopyroxenes (i.e. $[Ce/Y]_n \sim 8-13$) using I values similar to that
475 invoked in other magmatic settings worldwide ($\sim 4-10$; Lissenberg and MacLeod, 2016). Hence,
476 reactive porous flow represents a realistic mechanism for generating the geochemical diversity of
477 Floreana clinopyroxenes, including the trace element enriched crystals analysed in the wehrlitic
478 nodules (Fig. 9).

479 In addition, detailed LA-ICP-MS transects of two clinopyroxene grains from the most enriched
480 wehrlitic xenolith analysed in this study (17MMSG02c) show clear trace element zoning (Fig. 11).
481 The core of the larger clinopyroxene crystal has low $[Ce]$ and $[Ce/Y]_n$ contents that are approximately
482 in equilibrium with Floreana basalts (Harpp et al. 2014a; Fig. 11a), whereas the mantle is
483 characterised by increasing $[Ce]$ and $[Ce/Y]_n$ contents towards the rim. We interpret this as core
484 crystallisation from a melt with a trace element signature similar to that of erupted Floreana basalts
485 (Harpp et al., 2014a), followed by growth from a melt which became progressively enriched during
486 reactive porous flow (Fig. 11).

487 The mantle of the second, smaller xenolithic clinopyroxene shows a similar rim-ward increase in $[Ce]$
488 (interpreted as progressive melt enrichment during reactive porous flow). However, the $[Ce]$ and
489 $[Ce/Y]_n$ values of the crystal core are too high to be in equilibrium with erupted Floreana basalts (Fig.
490 11C). This is consistent with spot analyses of clinopyroxene cores in other crystals analysed in this
491 study. The high $[Ce]$ and $[Ce/Y]_n$ values in crystal cores cannot be explained by inward diffusion of
492 Ce, owing to significant differences in the diffusivities of Ce and Y and similar $[Ce]$ and $[Y]$ zoning
493 patterns in our two crystal transects (Fig. 11; Van Orman, 2001). Instead, we suggest that the high
494 apparent core $[Ce]$ and $[Ce/Y]_n$ contents in many of the Floreana clinopyroxenes record crystallisation
495 from melts that had already undergone geochemical enrichment via reactive porous flow. However,
496 we cannot discount that our apparent clinopyroxene cores are fragments of larger oikocrysts that have

497 been broken during mush disaggregation or sample crushing and, as a result, do not represent the true
498 core compositions of each crystal.

499 Nevertheless, our clinopyroxene major and trace element data, as well as petrographic observations of
500 the wehrlitic xenoliths, provide substantial evidence that reactive porous flow is an important
501 mechanism of melt migration and melt differentiation in highly crystalline magma storage regions
502 beneath Floreana. Although reactive porous flow has been identified as an important process in MOR
503 gabbros, this is the first study to identify reactive porous flow in an ocean island setting.

504 **6.4 Petrographic estimates of magma storage pressures**

505 Petrological and geophysical constraints on magma storage depths exist for several recently active
506 volcanoes in the western Galápagos Archipelago (Bagnardi et al., 2013; Case et al., 1973; Geist et al.,
507 1998; Stock et al., 2018; Vigouroux et al., 2008). However, in the absence of geophysical data (owing
508 to a paucity of recent eruptions), there are far fewer constraints on the structure of magma storage
509 regions in the eastern and south-eastern archipelago. To date, the only investigation of magma storage
510 depths beneath these volcanoes is by Geist et al. (1998), who undertook a visual comparison between
511 whole-rock lava compositions and the MORB olivine + plagioclase + augite + melt pseudoinvariant
512 point, parameterised by Grove et al. (1992). This approach is subject to substantial uncertainty, but the
513 authors suggest that Floreana magmas consistently equilibrate at >5 kbar (typically >7 kbar) at a
514 depth >16 km, within the upper mantle.

515 We used three petrological barometers to provide improved constraints on magma storage depths
516 beneath Floreana. First, we applied the clinopyroxene-only barometer of Putirka (2008), in which
517 pressure and temperature are solved iteratively based solely on the clinopyroxene major element
518 composition (primarily the jadeite component; standard error of estimate [SEE] = ± 310 MPa).

519 Second, we applied the clinopyroxene-melt barometer of Neave and Putirka (2017), which uses the
520 composition of a co-existing melt phase and the proportion of the Jadeite component in clinopyroxene
521 to calculate the pressure of crystallisation (SEE = ± 140 MPa; pressure is solved iteratively with
522 temperature using the clinopyroxene-melt thermometer of Putirka, 2008). Third, for the xenolithic

523 nodules, we estimate the final pressure and temperature of storage using the two-pyroxene
524 thermobarometer of Putirka (2008) ($SEE = \pm 260$ MPa).

525 Taken at face value, initial application of the clinopyroxene-only barometer to all clinopyroxene
526 analyses from the scoria and xenolith samples gives a range of pressure estimates between ~ 450 MPa
527 and ~ 1800 MPa. However, reactive porous flow has a substantial influence on the compositions of the
528 Group 1 (and Group 2) clinopyroxenes, which may influence the barometric results. Specifically,
529 crystals that show evidence for reactive porous flow also have elevated Na concentrations, leading to
530 an anomalously high jadite component. Therefore, we filter our dataset to remove crystals that show a
531 chemical signature indicative of reactive porous flow and only use Group 3 clinopyroxenes that have
532 trace element compositions in equilibrium with the Floreana basalts (using the whole-rock data from
533 Harpp et al. 2014) in our barometric calculations ($n=78$). Results indicate that crystallisation beneath
534 Floreana occurs at a pressure of 766 ± 322 MPa (2σ of calculated pressures), which equates to a depth
535 of 25.2 ± 9.9 km (using the crustal density estimate of Putirka (1997) and a mantle density estimate of
536 3300 km/m³; Fig. 12).

537 Application of the Neave and Putirka (2017) clinopyroxene-melt barometer requires identification of
538 equilibrium clinopyroxene-liquid pairs. We achieve this using an automated melt-matching algorithm
539 (as in Winpenny and MacLennan, 2011, Neave and Putirka, 2017, Stock et al. 2018), with $K_D(\text{Fe-Mg})$,
540 diopside-hedenbergite, enstatite-ferrosillite and calcium Tschermak's equilibrium tests ($K_D(\text{Fe-Mg})$
541 within ± 0.03 other components within 2 SEE; Putirka, 1999, Putirka, 2008, Mollo et al., 2013). We
542 used the whole-rock data of Harpp et al. (2014a) and basaltic glass analyses from this study as
543 potential equilibrium liquids. Input crystal compositions were again filtered to remove analyses that
544 showed evidence of reactive porous flow (i.e. only Group 3 clinopyroxenes in equilibrium with the
545 Floreana whole-rock were used). In total, 70 of the 78 input clinopyroxene analyses returned at least
546 one equilibrium match to either the basaltic glass or whole-rock compositions. Where clinopyroxene
547 compositions produced an equilibrium match with more than one equilibrium melt, an average melt
548 composition was used in the barometric model. Results from this barometer indicate that magma
549 crystallisation occurred at 717 ± 165 MPa (23.7 ± 5.1 km) and $1224 \pm 33^\circ\text{C}$ (Fig. 12).

550 Clinopyroxene-orthopyroxene thermobarometry records the final storage conditions of the cumulate
551 xenoliths, rather than the crystallisation conditions of clinopyroxene autocrysts (orthopyroxene is only
552 found as an intercumulus phase). Temperature and pressure estimates were only calculated from
553 orthopyroxene-clinopyroxene pairs in wehrlite and dunite xenoliths that passed the $K_D(\text{Fe-Mg})$
554 equilibrium test of Putirka (2008; within ± 0.14). Results suggest that the cumulates were stored at
555 $\sim 975\text{--}1100^\circ\text{C}$ and $600\text{--}900$ MPa, with a mean storage pressure of 712 ± 200 MPa (23.7 ± 6.4 km; Fig.
556 12).

557 The depths of magma storage calculated from our three petrological barometers show an excellent
558 agreement within the model uncertainties. These new data provide robust evidence that magma
559 storage beneath Floreana occurs below the Moho (~ 16 km; Feighner and Richards, 1994), in the upper
560 mantle.

561 **7 IMPLICATIONS FOR MAGMATIC PLUMBING** 562 **SYSTEMS BENEATH LOW MELT FLUX OCEAN** 563 **ISLAND VOLCANOES**

564 Our new petrological and geochemical data show that magma storage beneath Floreana occurs in
565 mush-dominated regions in the upper mantle (Fig. 13). Mineral chemistry (such as low olivine Ca
566 concentrations and clinopyroxene major elements) reveal that a substantial portion of the erupted
567 crystal cargo is derived from disaggregated mush and wall rock material which has been entrained
568 into the ascending magmas. During ascent, magmas may entrain coherent nodules (xenoliths) as well
569 as disaggregated mush (Fig. 13). Coherent nodules represent areas of the magmatic system beneath
570 Floreana that have undergone cooling to temperatures $< 1100^\circ\text{C}$ (compared to the clinopyroxene
571 crystallisation temperatures of $\sim 1225^\circ\text{C}$) and may represent material from the border of the active
572 mush zone or older, almost completely solidified magma storage regions that are intersected during
573 magma ascent (Fig. 13).

574 Petrographic observations and clinopyroxene trace element chemistry from both the xenolith and
575 scoria samples reveal that clinopyroxene growth occurs via reactive porous flow in the mush-

576 dominated areas beneath Floreana. Reactive porous flow causes distinct trace element enrichment in
577 the percolating melt phase and crystallising clinopyroxene, which can explain the trace element
578 disequilibrium between the erupted Floreana basalts and their clinopyroxene cargo. Nevertheless, the
579 presence of some clinopyroxene crystals with major and trace element compositions in equilibrium
580 with erupted Floreana basalts indicates that at least some crystallisation occurs in liquid-rich sub-
581 volcanic storage regions, likely situated as localised melt pockets within the larger mush zone (Fig.
582 13). Transport of melts modified by reactive porous flow into these melt pockets could impact the
583 LREE enriched signature of the resultant hybridised melts. This could explain the LREE-enriched
584 signature in the Floreana basalts, which is not seen in other regions of the Galápagos Archipelago
585 (Harpp et al., 2014a).

586 Our results indicate substantial differences in the architecture of the magmatic systems beneath
587 Floreana and the frequently active shield volcanoes in the western Galápagos Archipelago. For
588 example, previous petrological and geophysical studies have identified that western Galápagos
589 magmatic systems are characterised by crustal magma storage, often with a large storage region in the
590 mid-to-lower crust (~7 km depth) and a smaller storage region at shallow levels, within the volcanic
591 edifice (~1 km depth; Geist et al. 1998; Bagnardi et al. 2013; Bagnardi and Hooper, 2018; Stock et al.,
592 2018; Fig 12). In contrast, our barometric data indicate that magmas beneath Floreana ascend directly
593 from the upper mantle and undergo no detectable crustal storage. Although mush-rich regions have
594 been inferred beneath the western Galápagos shield volcanoes (based on whole-rock data and the
595 presence of gabbroic glomerocrysts; Chadwick et al., 2011; Geist et al., 1995, 2014; Stock et al.,
596 2018), magmatic differentiation appears to be driven by simple fractional crystallisation and mixing
597 of chemically diverse magmas (Geist et al., 1995; Naumann and Geist, 1999; Stock et al., *in review*).

598 One major factor that differentiates Floreana from shield volcanoes in the western archipelago (on
599 Isabela and Fernandina) is the flux of magma into the lithosphere, as evidenced by variations in the
600 volumetric eruption rate (Harpp et al., 2014a; Harpp and Geist, 2018; Kurz et al., 2014). Hence, we
601 suggest that the greater pressure of magma storage and prevalence of reactive porous flow beneath
602 Floreana, relative to volcanoes in the western archipelago, are related to the substantially lower flux of

603 magma into the lithosphere from the underlying mantle source (and thus the thermal structure of the
604 lithosphere). For example, the magma flux entering the lithosphere beneath Wolf volcano (northern
605 Isabela) has been substantially greater than that beneath Floreana for several 100,000s of years. The
606 high magma flux beneath Wolf maintains the average temperature of the mid-to-lower crust at
607 $\sim 1125^{\circ}\text{C}$ ($\Delta T \sim 22^{\circ}\text{C}$), with only small-scale thermal and compositional heterogeneities present in the
608 sub-volcanic plumbing system (Geist et al., 2014, 2005; Stock et al., 2018, *in review*). In contrast, the
609 flux of magma entering the magmatic system beneath Floreana is much lower and the temperature of
610 the mid-crust is likely to be $\ll 800^{\circ}\text{C}$ (i.e. significantly cooler than the lowest temperature recorded by
611 the Floreana xenoliths; Fig. 12). As the flux of magma (and heat) from the mantle is insufficient to
612 maintain an elevated crustal geotherm beneath Floreana, magmas that stall in the crust are likely to
613 rapidly crystallise, increase their viscosity, and become uneruptable. Therefore, eruptions must be fed
614 by melts ascending from much deeper storage regions ($\sim 700\text{-}750$ MPa) where super-solidus melts can
615 persist over long time periods.

616 Our results have global implications for the architecture and dynamics of magma storage regions
617 beneath ocean island volcanoes that are characterised by a relatively low flux of magma from the
618 underlying mantle. These include off-axis volcanic systems (e.g. Halekala, Hawaii) and those above
619 low buoyancy flux mantle plumes (e.g. El Hierro, Canary Islands). Figure 14 shows a compilation of
620 published barometric estimates from 'high' and 'low' melt flux systems in some of the most active
621 ocean island systems on Earth (Hawaii, Iceland and Galápagos; Hammer et al., 2016; Hartley et al.,
622 2018; Neave and Putirka, 2017; Poland et al., 2015; Stock et al., 2018). Central volcanic systems from
623 each region typically display relatively low-pressure magma storage compared to regions that are
624 characterised by a comparatively low magma flux from the convecting mantle (i.e. off-axis volcanic
625 systems; Fig. 14). This observation is consistent with the high pressures of magma storage identified
626 at other ocean island volcanoes that are located above mantle plumes with a relatively low buoyancy
627 flux (e.g. $>15\text{-}25$ km at El Hierro in the Canary Islands; Longpre et al., 2014; Taracsák et al., 2019).
628 Hence, we speculate that high-pressure magma storage is characteristic of low melt flux ocean island
629 volcanoes globally.

630 **8 CONCLUSIONS**

631 Petrographic and geochemical analyses of lava, scoria and xenolith samples from Floreana in the
632 south-eastern Galápagos Archipelago provide new insights into the architecture and dynamics of
633 magma storage beneath low melt flux ocean island volcanoes. Comparison of olivine and
634 clinopyroxene major, minor and trace element contents between our different sample types reveals
635 that a substantial portion of the erupted crystal cargo is derived from mush-dominated magma storage
636 regions beneath Floreana. Mineral textures, highly enriched clinopyroxene trace element signatures
637 and trace element zoning in the xenoliths reveals that reactive porous flow is an important process of
638 chemical differentiation and melt transport within these mush-dominated regions. Mixing between
639 melts that have been geochemically enriched by reactive porous flow and those in overlying liquid-
640 rich storage regions could explain the anomalous LREE enriched signature of the Floreana basalts,
641 which is absent in other parts of the Galápagos Archipelago where reactive porous flow has not been
642 identified.

643 Application of independent petrological barometers to crystals in Floreana scoria and xenolith
644 samples indicates that magmas are stored in the upper mantle ($\sim 23.7 \pm 5.1$ km). Floreana is in a distal
645 location to the Galápagos plume where the melt flux entering the lithosphere is low; the depth of
646 magma storage beneath Floreana contrasts with more proximal, higher melt flux volcanoes in the
647 western archipelago where magmas are stored in the crust (Geist et al., 1998; Stock et al., 2018).
648 Comparing our new data with ocean island volcanoes globally (e.g. Hawaii, Iceland and the Canary
649 Islands) reveals that the Galápagos is not unique and that magma storage is ubiquitously shallower in
650 proximal magmatic systems above high buoyancy flux plumes than in off-axis systems, or above low
651 buoyancy flux plumes. We therefore suggest that the flux of mantle-derived magma entering the
652 lithosphere imparts a first-order control on the depth of magma storage beneath ocean island
653 volcanoes.

654 **ACKNOWLEDGEMENTS**

655 This study was supported by a NERC (Natural Environmental Research Council) Research Training
656 Student Grant (NE/L002507/1) awarded to M.L.M.G as well as NERC grant awarded to S.A.G

657 RG57434. M. J. S. was supported by a Charles Darwin and Galápagos Islands Junior Research
658 Fellowship at Christ's College, Cambridge. We are grateful to Iris Buisman and Jason Day for their
659 help with electron microprobe and laser-ablation inductively-coupled mass spectrometry analysis,
660 respectively. We also thank Dr Margaret Hartley for her comments on an early version of this
661 manuscript. We are also grateful to the Charles Darwin Foundation and the Galapagos National Park
662 authorities for their help during fieldwork.

663 REFERENCES

- 664 Adams, G.E., Bishop, F.C., 1982. Experimental investigation of CaMg exchange between olivine,
665 orthopyroxene, and clinopyroxene: potential for geobarometry. *Earth Planet. Sci. Lett.* 57,
666 241–250. [https://doi.org/10.1016/0012-821X\(82\)90188-1](https://doi.org/10.1016/0012-821X(82)90188-1)
- 667 Allan, J.F., Simkin, T., 2000. Fernandina Volcano's evolved, well-mixed basalts: Mineralogical and
668 petrological constraints on the nature of the Galápagos plume. *J. Geophys. Res. Solid Earth*
669 105, 6017–6041. <https://doi.org/10.1029/1999JB900417>
- 670 Amelung, F., Jónsson, S., Zebker, H., Segall, P., 2000. Widespread uplift and 'trapdoor' faulting on
671 Galápagos volcanoes observed with radar interferometry. *Nature* 407, 993–996.
672 <https://doi.org/10.1038/35039604>
- 673 Asimow, P.D., Langmuir, C.H., 2003. The importance of water to oceanic mantle melting regimes.
674 *Nature* 421, 815–820. <https://doi.org/10.1038/nature01429>
- 675 Bagnardi, M., Amelung, F., Poland, M.P., 2013. A new model for the growth of basaltic shields based
676 on deformation of Fernandina volcano, Galápagos Islands. *Earth Planet. Sci. Lett.* 377–378,
677 358–366. <https://doi.org/10.1016/j.epsl.2013.07.016>
- 678 Bailey, K., 1976. Potassium-Argon Ages from the Galápagos Islands. *Science* 192, 465–467.
679 <https://doi.org/10.1126/science.192.4238.465>
- 680 Barker, S.J., Rowe, M.C., Wilson, C.J.N., Gamble, J.A., Rooyackers, S.M., Wysoczanski, R.J.,
681 Illsley-Kemp, F., Kenworthy, C.C., 2020. What lies beneath? Reconstructing the primitive
682 magmas fueling voluminous silicic volcanism using olivine-hosted melt inclusions.
- 683 Case, J.E., Ryland, S.L., Simkin, T., Howard, K.A., 1973. Gravitational Evidence for a Low-Density
684 Mass beneath the Galápagos Islands. *Science* 181, 1040–1042.
685 <https://doi.org/10.1126/science.181.4104.1040>
- 686 Chadwick, W.W., Howard, K.A., 1991. The pattern of circumferential and radial eruptive fissures on
687 the volcanoes of Fernandina and Isabela islands, Galápagos. *Bull. Volcanol.* 53, 259–275.
688 <https://doi.org/10.1007/BF00414523>
- 689 Chadwick, W.W., Jónsson, S., Geist, D.J., Poland, M., Johnson, D.J., Batt, S., Harpp, K.S., Ruiz, A.,
690 2011. The May 2005 eruption of Fernandina volcano, Galápagos: The first circumferential
691 dike intrusion observed by GPS and InSAR. *Bull. Volcanol.* 73, 679–697.
692 <https://doi.org/10.1007/s00445-010-0433-0>
- 693 Chakraborty, S., 2010. Diffusion Coefficients in Olivine, Wadsleyite and Ringwoodite. *Rev. Mineral.*
694 *Geochem.* 72, 603–639. <https://doi.org/10.2138/rmg.2010.72.13>
- 695 Clague, D.A., Denlinger, R.P., 1994. Role of olivine cumulates in destabilizing the flanks of Hawaiian
696 volcanoes. *Bull. Volcanol.* 56, 425–434. <https://doi.org/10.1007/BF00302824>
- 697 Cleary, Z., Schwartz, D.M., Mittelstaedt, E., Harpp, K., 2020. Dynamic Magma Storage at Near-
698 Ridge Hot Spots: Evidence From New Galápagos Gravity Data. *Geochem. Geophys.*
699 *Geosystems* 21. <https://doi.org/10.1029/2019GC008722>
- 700 Coogan, L.A., Saunders, A.D., Kempton, P.D., Norry, M.J., 2000. Evidence from oceanic gabbros for
701 porous melt migration within a crystal mush beneath the Mid-Atlantic Ridge. *Geochem.*
702 *Geophys. Geosystems* 1, n/a-n/a. <https://doi.org/10.1029/2000GC000072>
- 703 Costa, F., Shea, T., Ubide, T., 2020. Diffusion chronometry and the timescales of magmatic
704 processes. *Nat. Rev. Earth Environ.* <https://doi.org/10.1038/s43017-020-0038-x>
- 705 Davidge, L., Ebinger, C., Ruiz, M., Tepp, G., Amelung, F., Geist, D., Coté, D., Anzieta, J., 2017.
706 Seismicity patterns during a period of inflation at Sierra Negra volcano, Galápagos Ocean
707 Island Chain. *Earth Planet. Sci. Lett.* 462, 169–179. <https://doi.org/10.1016/j.epsl.2016.12.021>

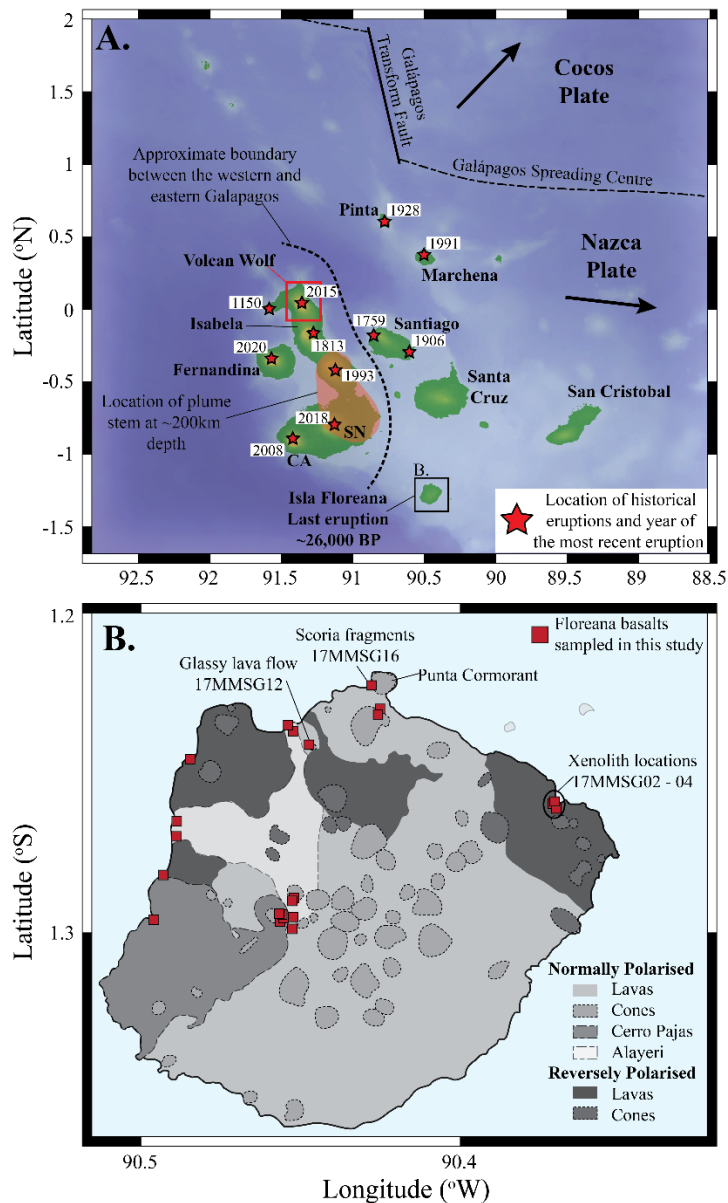
- 708 Donaldson, C.H., 1976. An experimental investigation of olivine morphology. *Contrib. Mineral.*
709 *Petrol.* 57, 187–213. <https://doi.org/10.1007/BF00405225>
- 710 Feighner, M.A., Richards, M.A., 1994. Lithospheric structure and compensation mechanisms of the
711 Galápagos Archipelago. *J. Geophys. Res.* 99, 6711. <https://doi.org/10.1029/93JB03360>
- 712 Gao, Y., Hoefs, J., Hellebrand, E., von der Handt, A., Snow, J.E., 2007. Trace element zoning in
713 pyroxenes from ODP Hole 735B gabbros: diffusive exchange or synkinematic crystal
714 fractionation? *Contrib. Mineral. Petrol.* 153, 429–442. [https://doi.org/10.1007/s00410-006-](https://doi.org/10.1007/s00410-006-0158-4)
715 0158-4
- 716 Gavrilenko, M., Herzberg, C., Vidito, C., Carr, M.J., Tenner, T., Ozerov, A., 2016. A Calcium-in-
717 Olivine Geohygrometer and its Application to Subduction Zone Magmatism. *J. Petrol.* 57,
718 1811–1832. <https://doi.org/10.1093/petrology/egw062>
- 719 Geist, D., Howard, K.A., Larson, P., 1995. The Generation of Oceanic Rhyolites by Crystal
720 Fractionation: the Basalt-Rhyolite Association at Volc n Alcedo, Galápagos Archipelago. *J.*
721 *Petrol.* 36, 965–982. <https://doi.org/10.1093/petrology/36.4.965>
- 722 Geist, D., Naumann, T., Larson, P., 1998. Evolution of Galápagos Magmas: Mantle and Crustal
723 Fractionation without Assimilation. *J. Petrol.* 39, 953–971.
724 <https://doi.org/10.1093/ptroj/39.5.953>
- 725 Geist, D., White, W.M., Albarede, F., Harpp, K., Reynolds, R., Blichert-Toft, J., Kurz, M.D., 2002.
726 Volcanic evolution in the Galápagos: The dissected shield of Volcan Ecuador. *Geochem.*
727 *Geophys. Geosystems* 3, 1 of 32–32 32. <https://doi.org/10.1029/2002GC000355>
- 728 Geist, D.J., Bergantz, G., Chadwick, W.W., 2014. Galápagos Magma Chambers, in: Harpp, K.S.,
729 Mittelstaedt, E., d’Ozouville, N., Graham, D.W. (Eds.), *Geophysical Monograph Series*. John
730 Wiley & Sons, Inc, Hoboken, New Jersey, pp. 55–69.
731 <https://doi.org/10.1002/9781118852538.ch5>
- 732 Geist, D.J., Fornari, D.J., Kurz, M.D., Harpp, K.S., Adam Soule, S., Perfit, M.R., Koleszar, A.M.,
733 2006. Submarine Fernandina: Magmatism at the leading edge of the Galápagos hot spot.
734 *Geochem. Geophys. Geosystems* 7, n/a-n/a. <https://doi.org/10.1029/2006GC001290>
- 735 Geist, D.J., McBIRNEY, A.R., Duncan, R.A., 1986. Geology and petrogenesis of lavas from San
736 Cristobal Island, Galápagos Archipelago. *Geol. Soc. Am. Bull.* 97, 555.
737 [https://doi.org/10.1130/0016-7606\(1986\)97<555:GAPOLF>2.0.CO;2](https://doi.org/10.1130/0016-7606(1986)97<555:GAPOLF>2.0.CO;2)
- 738 Geist, D.J., Naumann, T.R., Standish, J.J., Kurz, M.D., Harpp, K.S., White, W.M., Fornari, D.J.,
739 2005. Wolf Volcano, Galápagos Archipelago: Melting and Magmatic Evolution at the
740 Margins of a Mantle Plume. *J. Petrol.* 46, 2197–2224.
741 <https://doi.org/10.1093/petrology/egi052>
- 742 Geist, D.J., White, W.M., McBirney, A.R., 1988. Plume-asthenosphere mixing beneath the Galápagos
743 archipelago. *Nature* 333, 657–660. <https://doi.org/10.1038/333657a0>
- 744 Gibson, S.A., Dale, C.W., Geist, D.J., Day, J.A., Brüggmann, G., Harpp, K.S., 2016. The influence of
745 melt flux and crustal processing on Re–Os isotope systematics of ocean island basalts:
746 Constraints from Galápagos. *Earth Planet. Sci. Lett.* 449, 345–359.
747 <https://doi.org/10.1016/j.epsl.2016.05.021>
- 748 Gibson, S.A., Geist, D., 2010. Geochemical and geophysical estimates of lithospheric thickness
749 variation beneath Galápagos. *Earth Planet. Sci. Lett.* 300, 275–286.
750 <https://doi.org/10.1016/j.epsl.2010.10.002>
- 751 Gibson, S.A., Geist, D.G., Day, J.A., Dale, C.W., 2012. Short wavelength heterogeneity in the
752 Galápagos plume: Evidence from compositionally diverse basalts on Isla Santiago. *Geochem.*
753 *Geophys. Geosystems* 13. <https://doi.org/10.1029/2012GC004244>
- 754 Gleeson, M.L.M., Gibson, S.A., 2019. Crustal controls on apparent mantle pyroxenite signals in
755 ocean-island basalts. *Geology*. <https://doi.org/10.1130/G45759.1>
- 756 Gleeson, M.L.M., Gibson, S.A., Williams, H.M., 2020. Novel insights from Fe-isotopes into the
757 lithological heterogeneity of Ocean Island Basalts and plume-influenced MORBs. *Earth*
758 *Planet. Sci. Lett.* 535, 116114. <https://doi.org/10.1016/j.epsl.2020.116114>
- 759 Grove, T.L., Kinzler, R.J., Bryan, W.B., 1992. Fractionation of Mid-Ocean Ridge Basalt (MORB), in:
760 Morgan, J.P., Blackman, D.K., Sinton, J.M. (Eds.), *Geophysical Monograph Series*. American
761 Geophysical Union, Washington, D. C., pp. 281–310. <https://doi.org/10.1029/GM071p0281>

- 762 Hammer, J., Jacob, S., Welsch, B., Hellebrand, E., Sinton, J., 2016. Clinopyroxene in postshield
763 Haleakala ankaramite: 1. Efficacy of thermobarometry. *Contrib. Mineral. Petrol.* 171, 7.
764 <https://doi.org/10.1007/s00410-015-1212-x>
- 765 Harpp, K.S., Geist, D.J., 2018. The Evolution of Galápagos Volcanoes: An Alternative Perspective.
766 *Front. Earth Sci.* 6. <https://doi.org/10.3389/feart.2018.00050>
- 767 Harpp, K.S., Geist, D.J., Koleszar, A.M., Christensen, B., Lyons, J., Sabga, M., Rollins, N., 2014a.
768 The Geology and Geochemistry of Isla Floreana, Galápagos: A Different Type of Late-Stage
769 Ocean Island Volcanism, in: Harpp, K.S., Mittelstaedt, E., d'Ozouville, N., Graham, D.W.
770 (Eds.), *Geophysical Monograph Series*. John Wiley & Sons, Inc, Hoboken, New Jersey, pp.
771 71–117. <https://doi.org/10.1002/9781118852538.ch6>
- 772 Harpp, K.S., White, W.M., 2001. Tracing a mantle plume: Isotopic and trace element variations of
773 Galápagos seamounts. *Geochem. Geophys. Geosystems* 2, n/a-n/a.
774 <https://doi.org/10.1029/2000GC000137>
- 775 Harpp, K.S., Wirth, K.R., Teasdale, R., Blair, S., Reed, L., Barr, J., Pistiner, J., Korich, D., 2014b.
776 Plume-Ridge Interaction in the Galápagos: Perspectives from Wolf, Darwin, and Genovesa
777 Islands, in: Harpp, K.S., Mittelstaedt, E., d'Ozouville, N., Graham, D.W. (Eds.), *Geophysical*
778 *Monograph Series*. John Wiley & Sons, Inc, Hoboken, New Jersey, pp. 285–334.
779 <https://doi.org/10.1002/9781118852538.ch15>
- 780 Harris, P.G., 1957. Zone refining and the origin of potassic basalts. *Geochim. Cosmochim. Acta* 12,
781 195–208. [https://doi.org/10.1016/0016-7037\(57\)90032-7](https://doi.org/10.1016/0016-7037(57)90032-7)
- 782 Hartley, M.E., Bali, E., Maclennan, J., Neave, D.A., Halldórsson, S.A., 2018. Melt inclusion
783 constraints on petrogenesis of the 2014–2015 Holuhraun eruption, Iceland. *Contrib. Mineral.*
784 *Petrol.* 173. <https://doi.org/10.1007/s00410-017-1435-0>
- 785 Herzberg, C., 2011. Identification of Source Lithology in the Hawaiian and Canary Islands:
786 Implications for Origins. *J. Petrol.* 52, 113–146. <https://doi.org/10.1093/petrology/egq075>
- 787 Holness, M.B., Cheadle, M.J., McKenkie, D., 2005. On the Use of Changes in Dihedral Angle to
788 Decode Late-stage Textural Evolution in Cumulates. *J. Petrol.* 46, 1565–1583.
789 <https://doi.org/10.1093/petrology/egi026>
- 790 Holness, M.B., Nielsen, T.F.D., Tegner, C., 2006. Textural Maturity of Cumulates: a Record of
791 Chamber Filling, Liquidus Assemblage, Cooling Rate and Large-scale Convection in Mafic
792 Layered Intrusions. *J. Petrol.* 48, 141–157. <https://doi.org/10.1093/petrology/egl057>
- 793 Holness, M.B., Stock, M.J., Geist, D., 2019. Magma chambers versus mush zones: constraining the
794 architecture of sub-volcanic plumbing systems from microstructural analysis of crystalline
795 enclaves. *Philos. Trans. R. Soc. Math. Phys. Eng. Sci.* 377, 20180006.
796 <https://doi.org/10.1098/rsta.2018.0006>
- 797 Jackson, M.G., Konter, J.G., Becker, T.W., 2017. Primordial helium entrained by the hottest mantle
798 plumes. *Nature* 542, 340–343. <https://doi.org/10.1038/nature21023>
- 799 Jarosewich, E., Nelen, J.A., Norberg, J.A., 1980. Reference Samples for Electron Microprobe
800 Analysis*. *Geostand. Geoanalytical Res.* 4, 43–47. <https://doi.org/10.1111/j.1751-908X.1980.tb00273.x>
- 801
- 802 Jochum, K.P., Weis, U., Schwager, B., Stoll, B., Wilson, S.A., Haug, G.H., Andreae, M.O.,
803 Enzweiler, J., 2016. Reference Values Following ISO Guidelines for Frequently Requested
804 Rock Reference Materials. *Geostand. Geoanalytical Res.* 40, 333–350.
805 <https://doi.org/10.1111/j.1751-908X.2015.00392.x>
- 806 Kilbride, B.M., Edmonds, M., Biggs, J., 2016. Observing eruptions of gas-rich compressible magmas
807 from space. *Nat. Commun.* 7, 13744. <https://doi.org/10.1038/ncomms13744>
- 808 Köhler, T.P., Brey, G.P., 1990. Calcium exchange between olivine and clinopyroxene calibrated as a
809 geothermobarometer for natural peridotites from 2 to 60 kb with applications. *Geochim.*
810 *Cosmochim. Acta* 54, 2375–2388. [https://doi.org/10.1016/0016-7037\(90\)90226-B](https://doi.org/10.1016/0016-7037(90)90226-B)
- 811 Kurz, M.D., Rowland, S.K., Curtice, J., Saal, A.E., Naumann, T., 2014. Eruption Rates for Fernandina
812 Volcano: A New Chronology at the Galápagos Hotspot Center, in: Harpp, K.S., Mittelstaedt,
813 E., d'Ozouville, N., Graham, D.W. (Eds.), *Geophysical Monograph Series*. John Wiley &
814 Sons, Inc, Hoboken, New Jersey, pp. 41–54. <https://doi.org/10.1002/9781118852538.ch4>
- 815 Lissenberg, C.J., MacLeod, C.J., 2016. A Reactive Porous Flow Control on Mid-ocean Ridge
816 Magmatic Evolution. *J. Petrol.* 57, 2195–2220. <https://doi.org/10.1093/petrology/egw074>

- 817 Lissenberg, C.J., MacLeod, C.J., Howard, K.A., Godard, M., 2013. Pervasive reactive melt migration
818 through fast-spreading lower oceanic crust (Hess Deep, equatorial Pacific Ocean). *Earth*
819 *Planet. Sci. Lett.* 361, 436–447. <https://doi.org/10.1016/j.epsl.2012.11.012>
- 820 Longpre, M.-A., Klugel, A., Diehl, A., Stix, J., 2014. Mixing in mantle magma reservoirs prior to and
821 during the 2011–2012 eruption at El Hierro, Canary Islands. *Geology* 42, 315–318.
822 <https://doi.org/10.1130/G35165.1>
- 823 Lyons, J., Geist, D., Harpp, K., Diefenbach, B., Olin, P., Vervoort, J., 2007. Crustal growth by
824 magmatic overplating in the Galápagos. *Geology* 35, 511. <https://doi.org/10.1130/G23044A.1>
- 825 Matzen, A.K., Baker, M.B., Beckett, J.R., Wood, B.J., Stolper, E.M., 2017a. The effect of liquid
826 composition on the partitioning of Ni between olivine and silicate melt. *Contrib. Mineral.*
827 *Petrol.* 172. <https://doi.org/10.1007/s00410-016-1319-8>
- 828 Matzen, A.K., Wood, B.J., Baker, M.B., Stolper, E.M., 2017b. The roles of pyroxenite and peridotite
829 in the mantle sources of oceanic basalts. *Nat. Geosci.* 10, 530–535.
830 <https://doi.org/10.1038/ngeo2968>
- 831 Meyer, P.S., Dick, H.J.B., Thompson, G., 1989. Cumulate gabbros from the Southwest Indian Ridge,
832 54S–7 16 E: implications for magmatic processes at a slow spreading ridge. *Contrib. Mineral.*
833 *Petrol.* 103, 44–63. <https://doi.org/10.1007/BF00371364>
- 834 Mollo, S., Putirka, K., Misiti, V., Soligo, M., Scarlato, P., 2013. A new test for equilibrium based on
835 clinopyroxene–melt pairs: Clues on the solidification temperatures of Etnean alkaline melts at
836 post-eruptive conditions. *Chem. Geol.* 352, 92–100.
837 <https://doi.org/10.1016/j.chemgeo.2013.05.026>
- 838 Naumann, T., Geist, D., 2000. Physical volcanology and structural development of Cerro Azul
839 Volcano, Isabela Island, Galápagos: implications for the development of Galápagos-type
840 shield volcanoes. *Bull. Volcanol.* 61, 497–514. <https://doi.org/10.1007/s004450050001>
- 841 Naumann, T.R., Geist, D.J., 1999. Generation of alkalic basalt by crystal fractionation of tholeiitic
842 magma. *Geology* 27, 423. [https://doi.org/10.1130/0091-](https://doi.org/10.1130/0091-7613(1999)027<0423:GOABBC>2.3.CO;2)
843 [7613\(1999\)027<0423:GOABBC>2.3.CO;2](https://doi.org/10.1130/0091-7613(1999)027<0423:GOABBC>2.3.CO;2)
- 844 Neave, D.A., Namur, O., Shorttle, O., Holtz, F., 2019. Magmatic evolution biases basaltic records of
845 mantle chemistry towards melts from recycled sources. *Earth Planet. Sci. Lett.* 520, 199–211.
846 <https://doi.org/10.1016/j.epsl.2019.06.003>
- 847 Neave, D.A., Putirka, K.D., 2017. A new clinopyroxene–liquid barometer, and implications for
848 magma storage pressures under Icelandic rift zones. *Am. Mineral.* 102, 777–794.
849 <https://doi.org/10.2138/am-2017-5968>
- 850 Park, J., Morgan, J.K., Zelt, C.A., Okubo, P.G., Peters, L., Benesh, N., 2007. Comparative velocity
851 structure of active Hawaiian volcanoes from 3-D onshore–offshore seismic tomography.
852 *Earth Planet. Sci. Lett.* 259, 500–516. <https://doi.org/10.1016/j.epsl.2007.05.008>
- 853 Peterson, M.E., Saal, A.E., Kurz, M.D., Hauri, E.H., Blusztajn, J.S., Harpp, K.S., Werner, R., Geist,
854 D.J., 2017. Submarine Basaltic Glasses from the Galápagos Archipelago: Determining the
855 Volatile Budget of the Mantle Plume. *J. Petrol.* 58, 1419–1450.
856 <https://doi.org/10.1093/petrology/egx059>
- 857 Pietruszka, A.J., Heaton, D.E., Marske, J.P., Garcia, M.O., 2015. Two magma bodies beneath the
858 summit of Kīlauea Volcano unveiled by isotopically distinct melt deliveries from the mantle.
859 *Earth Planet. Sci. Lett.* 413, 90–100. <https://doi.org/10.1016/j.epsl.2014.12.040>
- 860 Poland, M.P., Miklius, A., Montgomery-Brown, E.K., 2015. Magma supply, storage, and transport at
861 shield stage Hawaiian volcanoes, in: *Characteristics of Hawaiian Volcanoes*.
- 862 Poldervaart, A., Hess, H.H., 1951. Pyroxenes in the Crystallization of Basaltic Magma. *J. Geol.* 59,
863 472–489. <https://doi.org/10.1086/625891>
- 864 Putirka, K., 1999. Clinopyroxene + liquid equilibria to 100 kbar and 2450 K. *Contrib. Mineral. Petrol.*
865 135, 151–163. <https://doi.org/10.1007/s004100050503>
- 866 Putirka, K., 1997. Magma transport at Hawaii: Inferences based on igneous thermobarometry 4.
- 867 Putirka, K.D., 2008. Thermometers and Barometers for Volcanic Systems. *Rev. Mineral. Geochem.*
868 69, 61–120. <https://doi.org/10.2138/rmg.2008.69.3>
- 869 Roeder, P.L., Emslie, R.F., 1970. Olivine–liquid equilibrium. *Contrib. Mineral. Petrol.* 29, 275–289.
870 <https://doi.org/10.1007/BF00371276>

- 871 Shejwalkar, A., Coogan, L.A., 2013. Experimental calibration of the roles of temperature and
872 composition in the Ca-in-olivine geothermometer at 0.1MPa. *Lithos* 177, 54–60.
873 <https://doi.org/10.1016/j.lithos.2013.06.013>
- 874 Sobolev, A.V., Hofmann, A.W., Kuzmin, D.V., Yaxley, G.M., Arndt, N.T., Chung, S.-L.,
875 Danyushevsky, L.V., Elliott, T., Frey, F.A., Garcia, M.O., Gurenko, A.A., Kamenetsky, V.S.,
876 Kerr, A.C., Krivolutsкая, N.A., Matvienkov, V.V., Nikogosian, I.K., Rocholl, A.,
877 Sigurdsson, I.A., Sushchevskaya, N.M., Teklay, M., 2007. The Amount of Recycled Crust in
878 Sources of Mantle-Derived Melts 316, 7.
- 879 Stock, M.J., Bagnardi, M., Neave, D.A., Maclennan, J., Bernard, B., Buisman, I., Gleeson, M.L.M.,
880 Geist, D., 2018. Integrated Petrological and Geophysical Constraints on Magma System
881 Architecture in the Western Galápagos Archipelago: Insights From Wolf Volcano. *Geochem.*
882 *Geophys. Geosystems* 19, 4722–4743. <https://doi.org/10.1029/2018GC007936>
- 883 Taracsák, Z., Hartley, M.E., Burgess, R., Edmonds, M., Iddon, F., Longpré, M.-A., 2019. High fluxes
884 of deep volatiles from ocean island volcanoes: Insights from El Hierro, Canary Islands.
885 *Geochim. Cosmochim. Acta* 258, 19–36. <https://doi.org/10.1016/j.gca.2019.05.020>
- 886 Thompson, R., 1987. Phase-equilibria constraints on the genesis and magmatic evolution of oceanic
887 basalts. *Earth-Sci. Rev.* 24, 161–210. [https://doi.org/10.1016/0012-8252\(87\)90023-7](https://doi.org/10.1016/0012-8252(87)90023-7)
- 888 Thompson, R.N., Gibson, S.A., 2000. Transient high temperatures in mantle plume heads inferred
889 from magnesian olivines in Phanerozoic picrites. *Nature* 407, 502–506.
890 <https://doi.org/10.1038/35035058>
- 891 Vidito, C., Herzberg, C., Gazel, E., Geist, D., Harpp, K., 2013. Lithological structure of the Galápagos
892 Plume: Lithological Structure Galpagos Plume. *Geochem. Geophys. Geosystems* 14, 4214–
893 4240. <https://doi.org/10.1002/ggge.20270>
- 894 Vigouroux, N., Williams-Jones, G., Chadwick, W., Geist, D., Ruiz, A., Johnson, D., 2008. 4D gravity
895 changes associated with the 2005 eruption of Sierra Negra volcano, Galápagos.
896 *GEOPHYSICS* 73, WA29–WA35. <https://doi.org/10.1190/1.2987399>
- 897 Villagómez, D.R., Toomey, D.R., Geist, D.J., Hooft, E.E.E., Solomon, S.C., 2014. Mantle flow and
898 multistage melting beneath the Galápagos hotspot revealed by seismic imaging. *Nat. Geosci.*
899 7, 151–156. <https://doi.org/10.1038/ngeo2062>
- 900 Wager, L.R., Brown, G.M., Wadsworth, W.J., 1960. Types of Igneous Cumulates. *J. Petrol.* 1, 73–85.
901 <https://doi.org/10.1093/petrology/1.1.73>
- 902 Welsch, B., Hammer, J., Hellebrand, E., 2014. Phosphorus zoning reveals dendritic architecture of
903 olivine. *Geology* 42, 867–870. <https://doi.org/10.1130/G35691.1>
- 904 White, W.M., McBirney, A.R., Duncan, R.A., 1993. Petrology and geochemistry of the Galápagos
905 Islands: Portrait of a pathological mantle plume. *J. Geophys. Res. Solid Earth* 98, 19533–
906 19563. <https://doi.org/10.1029/93JB02018>
- 907 Wieser, P.E., Edmonds, M., Maclennan, J., Jenner, F.E., Kunz, B.E., 2019. Crystal scavenging from
908 mush piles recorded by melt inclusions. *Nat. Commun.* 10, 5797.
909 <https://doi.org/10.1038/s41467-019-13518-2>
- 910 Wieser, P.E., Edmonds, M., Maclennan, J., Wheeler, J., 2020. Microstructural constraints on
911 magmatic mushes under Kīlauea Volcano, Hawai‘i. *Nat. Commun.* 11, 14.
912 <https://doi.org/10.1038/s41467-019-13635-y>
- 913 Winpenny, B., Maclennan, J., 2011. A Partial Record of Mixing of Mantle Melts Preserved in
914 Icelandic Phenocrysts. *J. Petrol.* 52, 1791–1812. <https://doi.org/10.1093/petrology/egr031>
- 915 Wood, B.J., Blundy, J.D., 1997. A predictive model for rare earth element partitioning between
916 clinopyroxene and anhydrous silicate melt. *Contrib. Mineral. Petrol.* 129, 166–181.
917 <https://doi.org/10.1007/s004100050330>
- 918

FIGURES



921

922 **Figure 1 - A.** Regional map of the Galápagos Archipelago highlighting the location of Isla Floreana,

923 Cerro Azul (CA), Sierra Negra (SN) and Wolf volcanoes. Dates show the most recent eruptions at

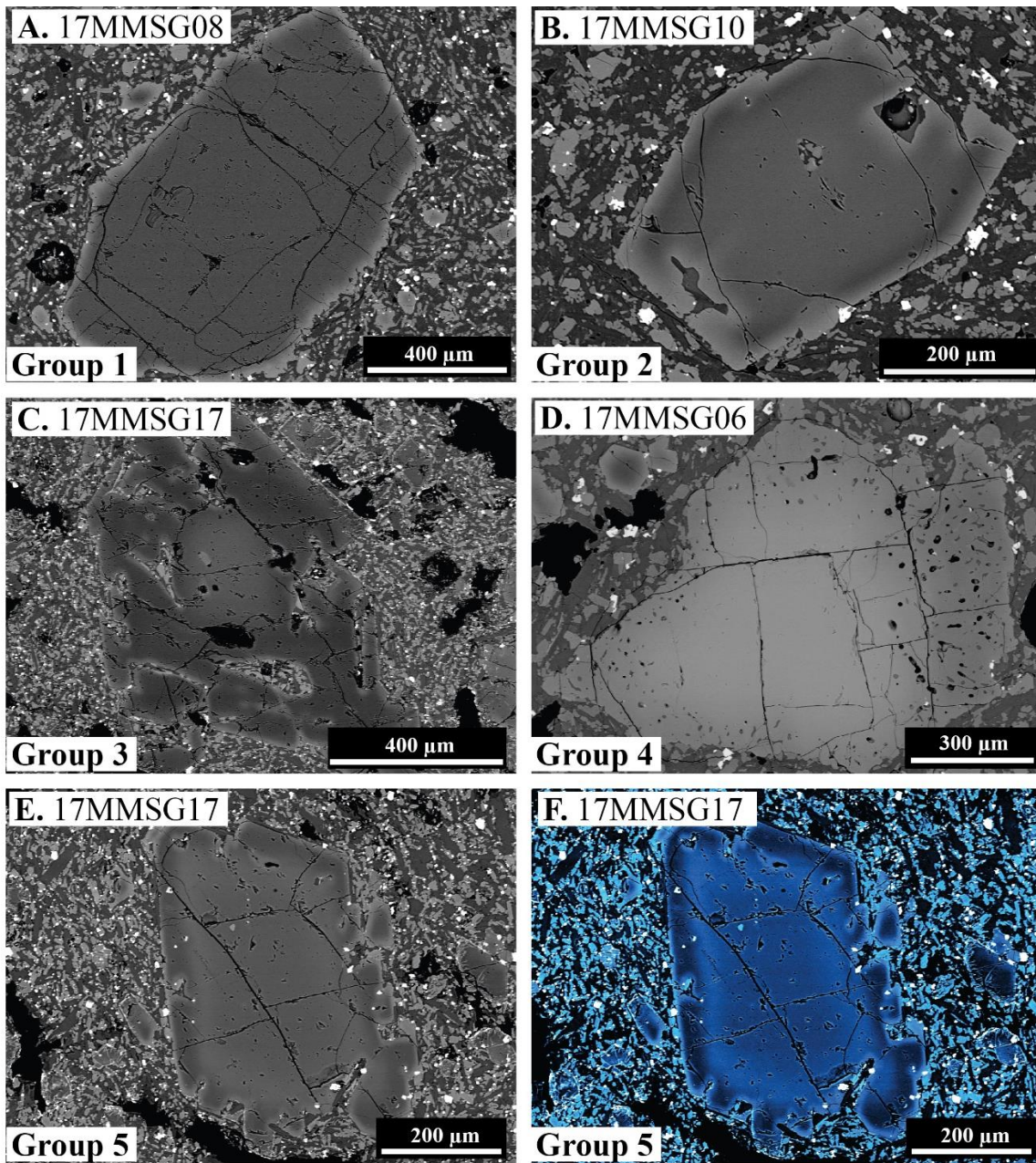
924 historically active volcanic centres. Black arrows show the direction of plate motion for the Nazca and

925 Cocos tectonic plates, respectively. **B.** Geological map of Floreana adapted from Harpp et al. (2014a).

926 Dashed lines delineate monogenetic scoria cones. Normally and reversely polarised lava flows are

927 shown along with the largest (Cerro Pajas) and most recent (Alayeri; ~26,000 years) eruptions on

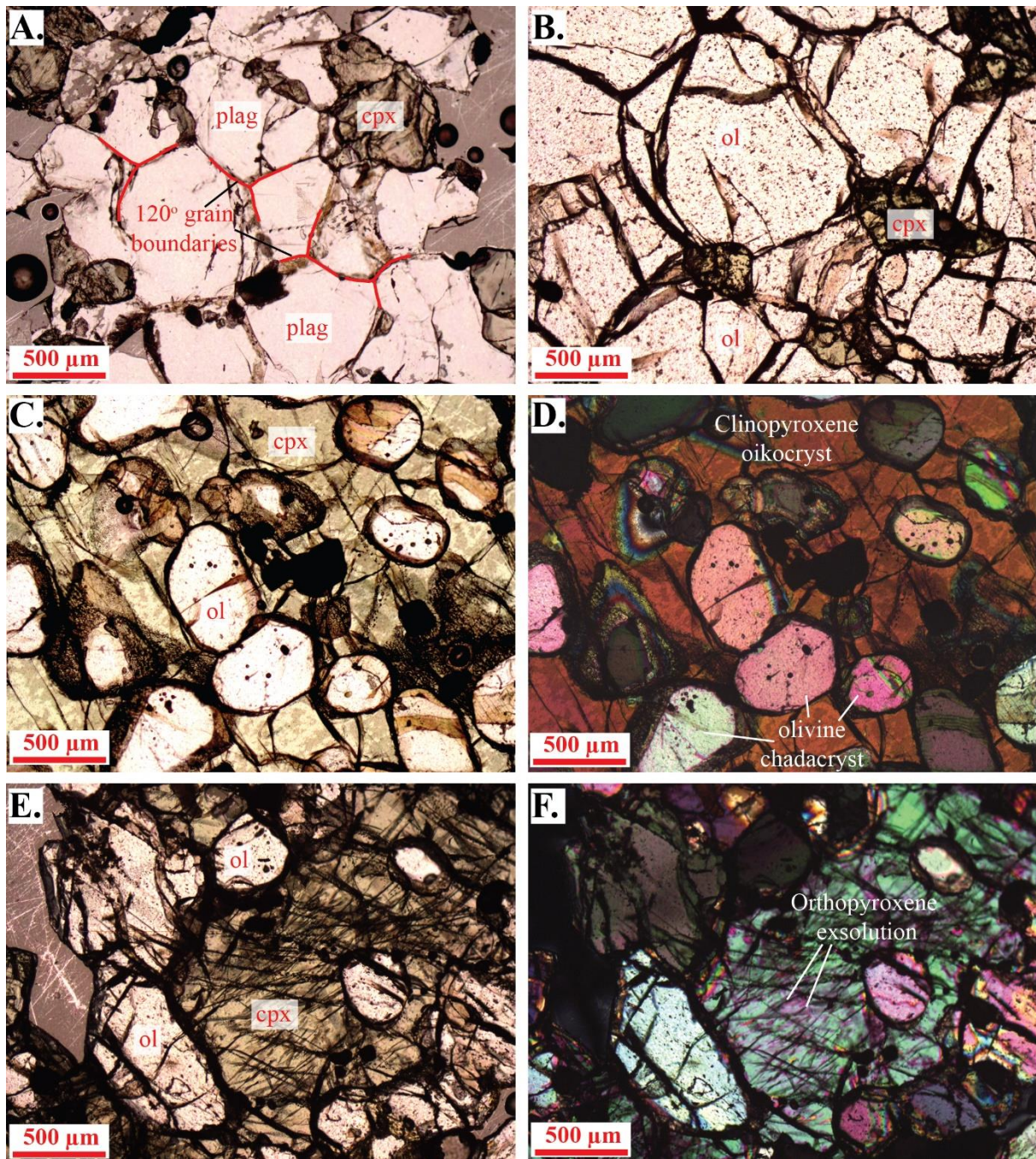
928 Floreana.



929

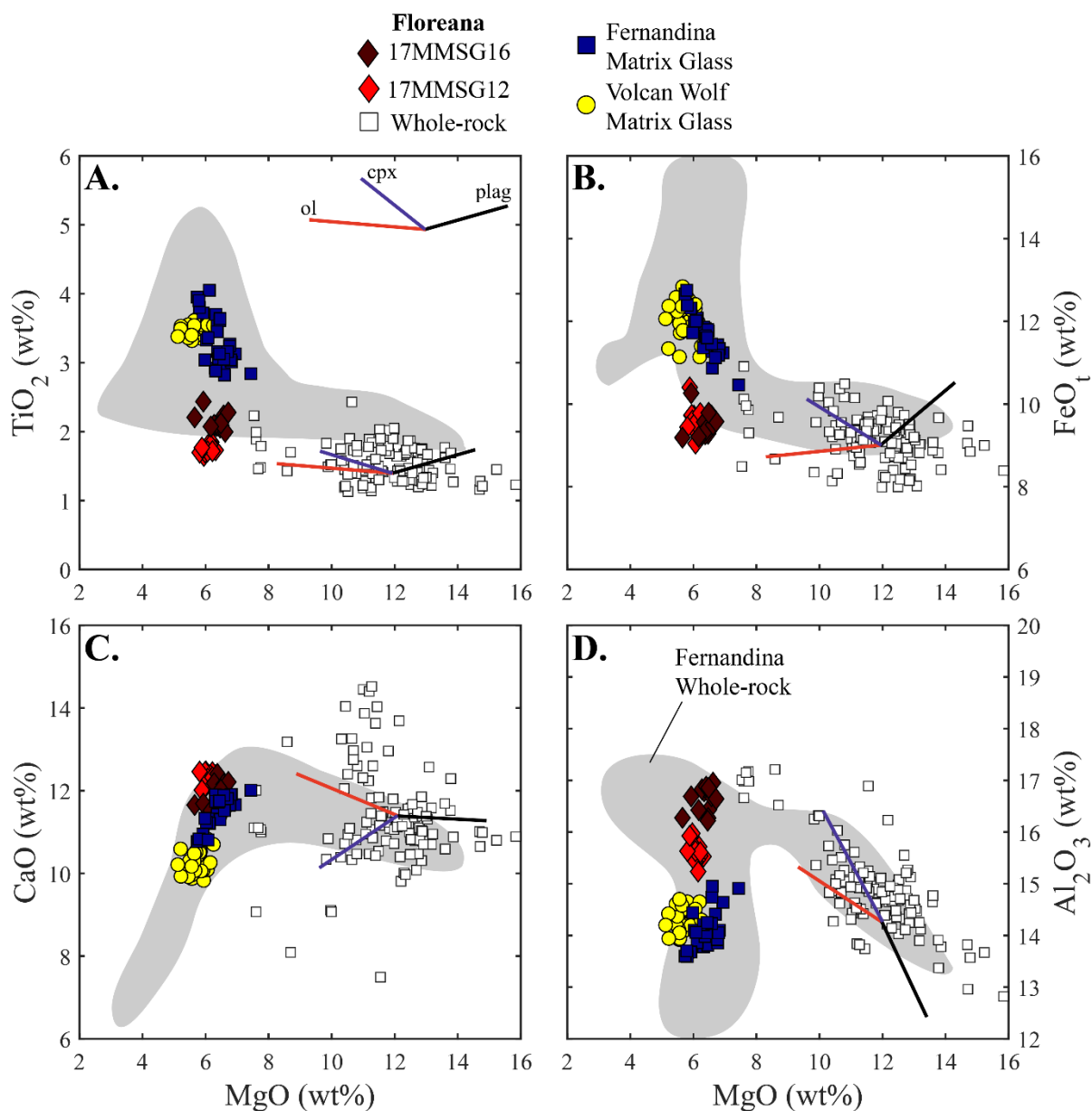
930 **Figure 2** - SEM images of **A.** Group 1 olivines – euhedral to subhedral crystal morphologies with
931 large, unzoned, crystal cores and narrow, normally-zoned rims. **B.** Group 2 olivines – subhedral to
932 euhedral crystals with clear, reverse-zoning profiles. **C.** Group 3 olivines – skeletal crystals with high
933 forsterite overgrowths on low forsterite cores. **D.** Group 4 olivines – anhedral crystals with sieved
934 textured, reverse zoned rims. **E.** (greyscale) and **F.** (false colour) Group 5 olivines – crystals preserve
935 at least 4 composition zones over ~100-200 μm .

936



937

938 **Figure 3** - Plane Polarised Light (A. – C. and E.) and Crossed Polarised Light (D., F.) images of
939 Floreana xenoliths. **A.** – gabbroic xenolith (17MMSG04b), highlighting near 120° grain boundaries at
940 monomineralic plagioclase (plag) triple junctions. **B.** – dunitic xenolith (17MMSG04c) with
941 intercumulus clinopyroxene growth. **C.** and **D.** – wehrlitic xenolith (17MMSG02c) showing a large
942 clinopyroxene (cpx) oikocryst surrounding olivine (ol) chadacrysts. **E.** and **F.** – wehrlitic xenolith
943 (sample 17MMSG03a) showing olivine chadacrysts within a clinopyroxene oikocryst. Orthopyroxene
944 exsolution lamellae are visible within the clinopyroxene.



945

946 **Figure 4** – Major element compositions of matrix glasses (this study) and whole-rocks (Harpp et al.,
947 2014a) from Floreana, as well as glasses from Fernandina (Peterson et al., 2017) and Wolf volcano
948 (Stock et al., 2018) in the western Galápagos Archipelago. Lines show trajectories of liquid
949 compositional evolution olivine (ol; red), clinopyroxene (cpx; blue) and plagioclase (plag; black)
950 crystallisation. The grey field shows whole-rock data from Isla Fernandina in the western Galápagos
951 (Allan and Simkin, 2000; Geist et al., 2006). The 2σ precision of our matrix glass analyses is smaller
952 than the symbol size.

953

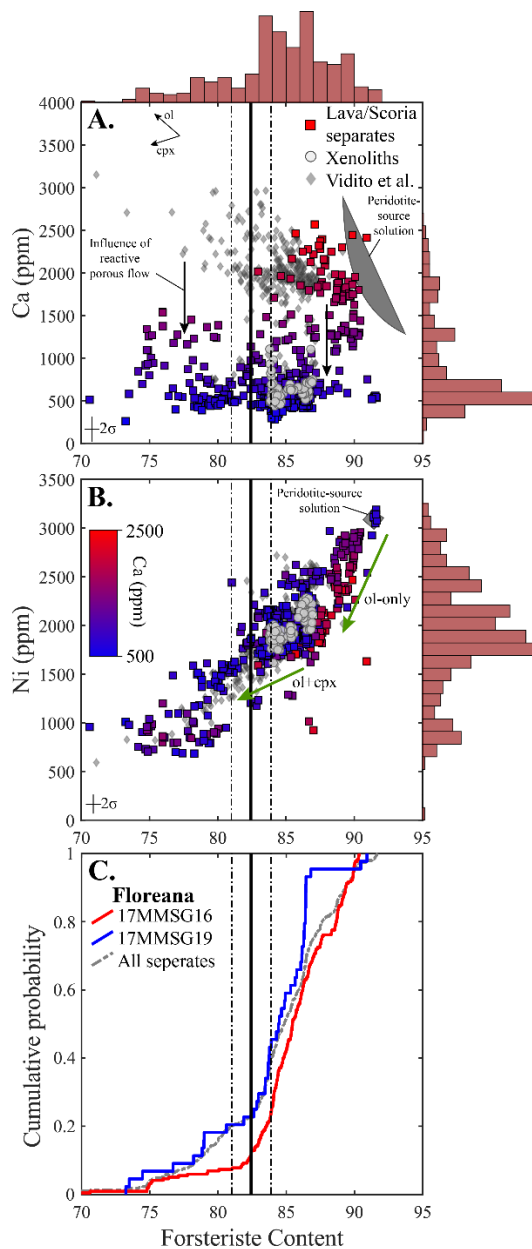
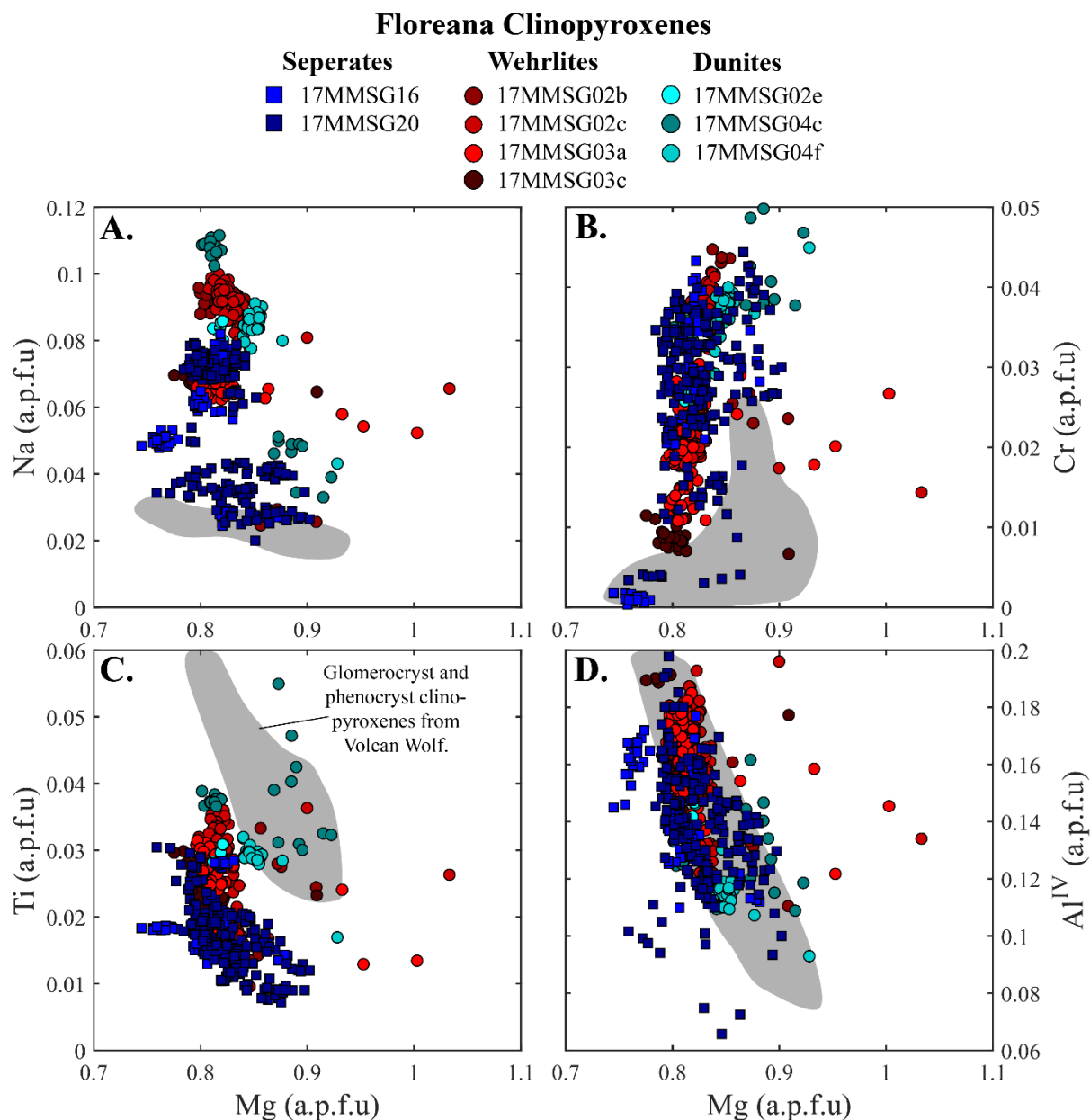


Figure 5 – Major and minor element compositions of olivine crystals from the Isla Floreana basalts. **A.** Fo vs. Ca and **B** Fo vs. Ni in Galápagos olivine crystals with analyses from our lava/scoria separates and xenolith samples, as well as a compilation of available olivine data from Floreana (Vidito et al. 2013). Our lava/scoria analyses are coloured according to their Ca concentration (see colour scale in **B**). The histograms above and to the right of the plots show the data distributions (excluding *in situ* analyses of xenolithic olivines). Peridotite source solutions are taken from Herzberg (2011) and Matzen et al. (2017a). Black arrows in **A.** show the trajectory of crystal compositional evolution during olivine (ol) and clinopyroxene (cpx) crystallisation (taken from Gleeson and Gibson, 2019) and the hypothesised influence of reactive porous flow. The green lines in

972 **B.** show the trajectories of crystal compositional evolution during olivine only, followed by olivine +
973 clinopyroxene fractional crystallisation (from Gleeson and Gibson, 2019). **C.** Cumulative probability
974 of forsterite in olivine separates from our lava (17MMSG19) and scoria (17MMSG16) samples. A
975 two-sample Kolmogorov-Smirnov test is used to assess the similarity of the forsterite distributions of
976 the two samples (and all analyses from lava and scoria deposits in this study). Results indicate that the
977 olivine populations from the two samples are drawn from the different distribution ($p=0.0021$). The
978 vertical black lines show the forsterite compositions of crystals calculated to be in equilibrium with
979 the matrix glass composition of tephra sample 17MMSG16 ($K_d = 0.30 \pm 0.03$ after Roeder and Emslie,
980 1970).

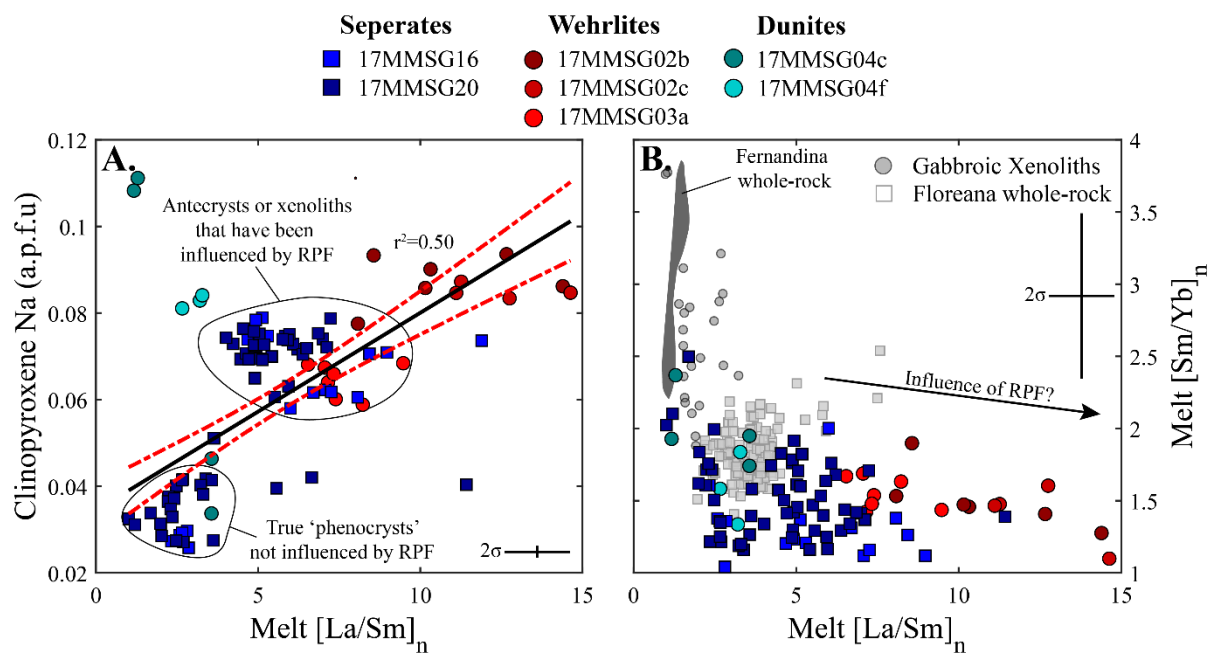


982 **Figure 6** – Major element composition of Floreana clinopyroxenes from our scoria samples and
983 wehrlite and dunite xenoliths. The grey field shows the compositions of clinopyroxenes from Wolf
984 volcano in the western Galápagos Archipelago (from Stock et al. 2018). The 2σ precision of our
985 clinopyroxene analyses is smaller than the symbol size.

986

987

988



989

990 **Figure 7 – A.** $[La/Sm]_n$ vs. Na in clinopyroxenes from our scoria samples and wehrlite and dunite
 991 xenoliths. The black line shows a regression through the data ($r^2 = 0.50$) and the red dashed lines
 992 show the 95% confidence limits on the regression. **B.** $[La/Sm]_n$ vs. $[Sm/Yb]_n$ of melts calculated to be
 993 in equilibrium with our Floreana clinopyroxenes using the model of Wood and Blundy (1997). The
 994 black arrow shows the approximate trend of crystal compositional evolution hypothesised to occur as
 995 a result of reactive porous flow. The grey field shows whole-rock compositions from Fernandina
 996 (Geist et al., 2006; White et al., 1993). **B** additionally shows the whole-rock compositions of erupted
 997 Floreana lavas (Harpp et al., 2014a) and analyses of the gabbroic xenoliths from Floreana (this study).
 998 Error bars show the fully propagated 2σ precision of our analyses.

999

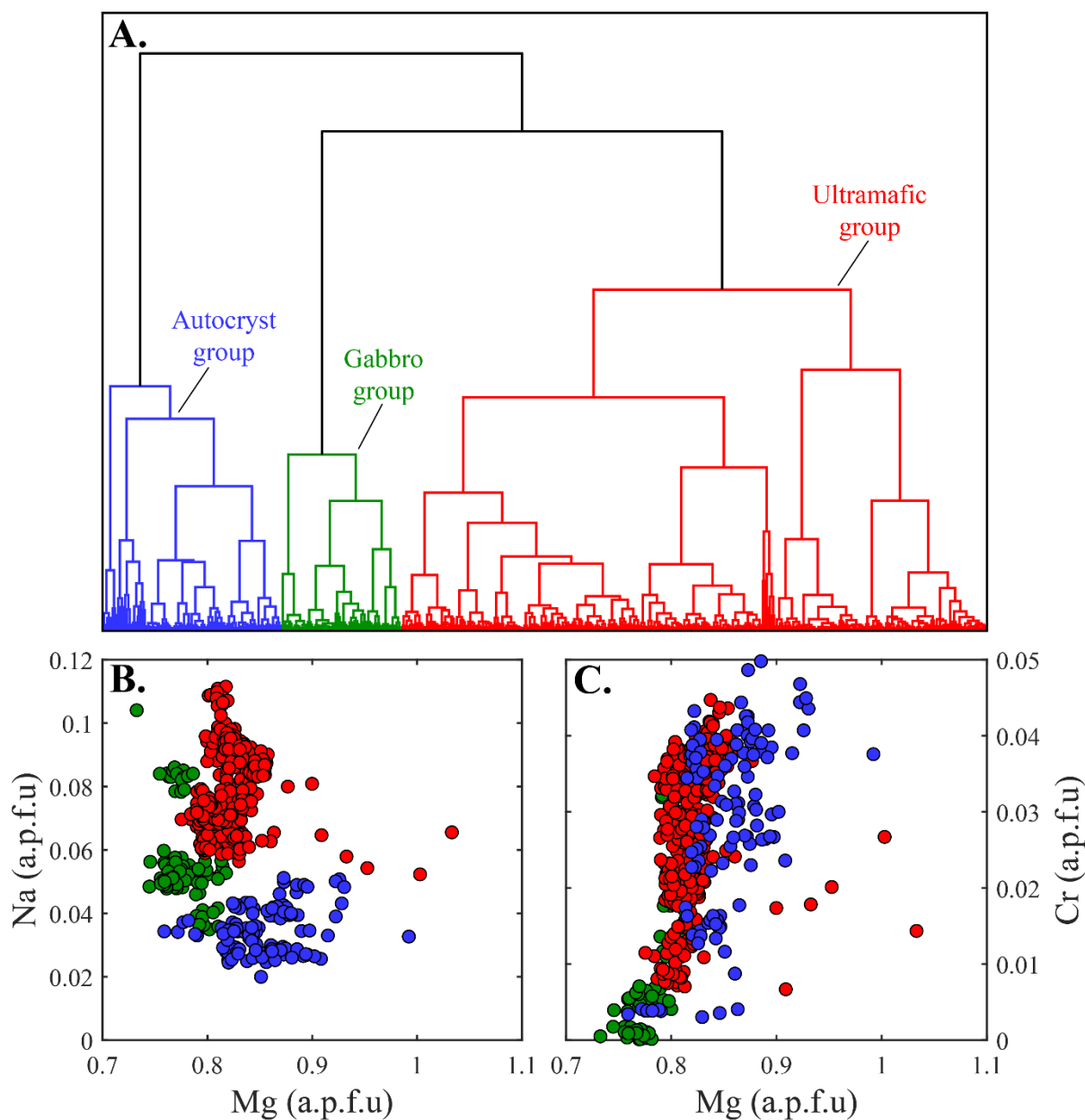
1000

1001

1002

1003

1004



1005

1006 **Figure 8** – A. Hierarchical cluster analysis of our clinopyroxene major element analyses. Colours

1007 show the high-level division of crystal compositions into three groups: Group 1 is predominantly

1008 comprised of crystals from wehrlite and dunite xenoliths (red), Group 2 is predominantly comprised

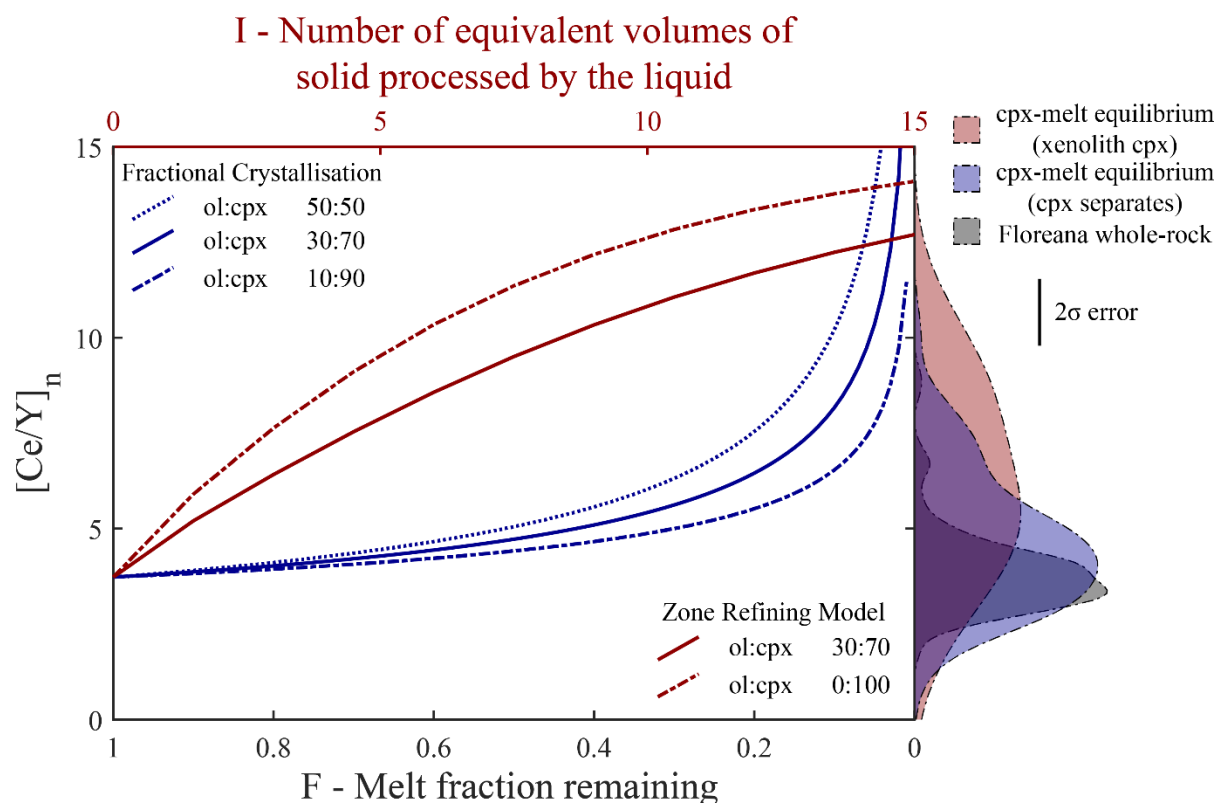
1009 of crystals from gabbroic xenoliths (green) and Group 3 (blue) is dominated by crystals separated

1010 from scoria samples. B Na vs Mg and C Cr vs Mg in our clinopyroxene analyses from the scoria and

1011 xenoliths, coloured by their group.

1012

1013

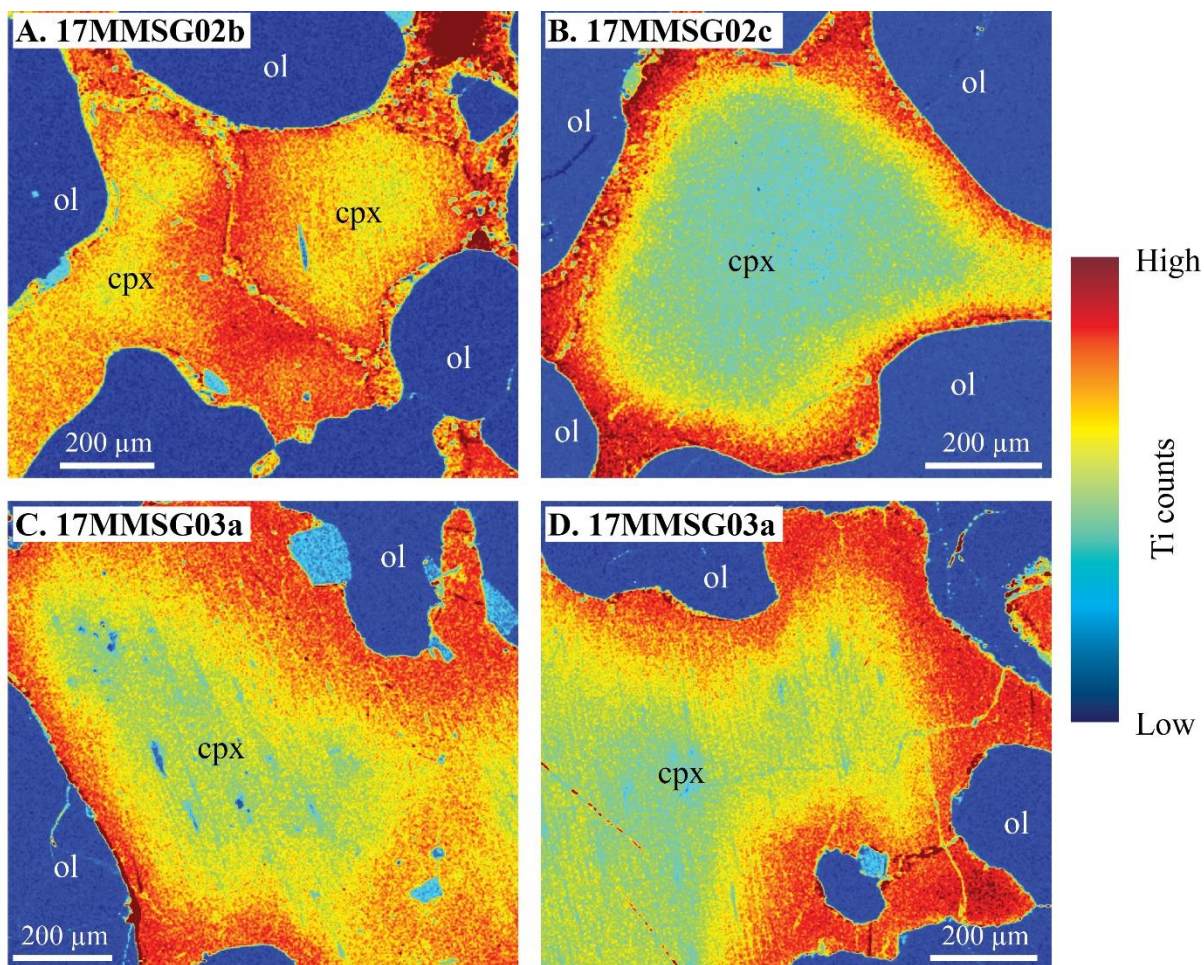


1014

1015 **Figure 9** – Models showing the evolution of melt $[Ce/Y]_n$ ratios as a function of the melt fraction
1016 remaining (F) during fractional crystallisation and as a function of the number of equivalent volumes
1017 of solid processed by the liquid (I) during reactive porous flow (red; using the zone-refining model of
1018 Harris, 1957). Line types show how models vary with different ratios of crystallising olivine (ol) and
1019 clinopyroxene (cpx). The kernel density plots to the right show the $[Ce/Y]_n$ density distributions of
1020 liquids calculated to be in equilibrium with clinopyroxene crystals in our wehrlite and dunite xenoliths
1021 (red), scoria samples (blue; 2σ error for the clinopyroxene analyses is shown by the black bar), and
1022 whole-rock analyses of erupted Floreana basalts (grey; Harpp et al., 2014a). Partition coefficients
1023 were calculated for clinopyroxene using the method of Wood and Blundy (1997), the mean major
1024 element composition of the group 3 clinopyroxenes from this study, a temperature of 1225°C, and a
1025 pressure of 700 MPa. Initial Ce and Y concentrations for both models were taken as the mean values
1026 from the whole-rock dataset of Harpp et al. (2014a). Calculation increments are 0.01 in F and 0.1 in I.

1027

1028



1029

1030 **Figure 10** – Ti maps of key clinopyroxene crystals in the Floreana wehrlite xenoliths. These maps
1031 display clear zoning in the xenolithic clinopyroxenes with Ti-poor cores and Ti-rich rims. The dark
1032 blue regions surrounding clinopyroxene grains are olivine crystals.

1033

1034

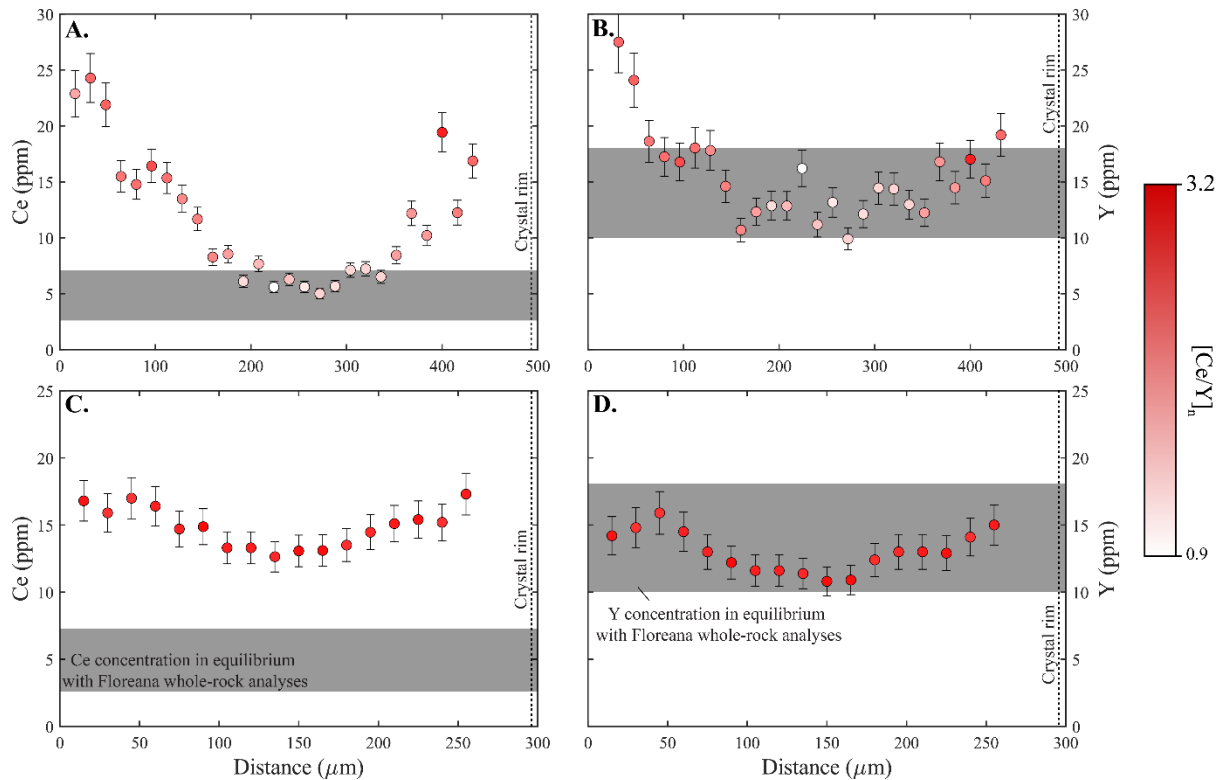
1035

1036

1037

1038

1039



1040

1041

Figure 11 – LA-ICP-MS transects showing Ce (**A, C**) and Y (**B, D**) zoning across two clinopyroxene grains in a wehrlitic xenolith (17MMSG02c). **A.** and **B.** show a transect across the core of a large clinopyroxene oikocryst. **C.** and **D.** show a transect across the apparent core of a smaller clinopyroxene oikocryst. Points are coloured according to their $[\text{Ce}/\text{Y}]_n$ ratio (see colour scale). The grey bars show the crystal compositions calculated to be in equilibrium with whole-rock analyses of erupted Floreana basalts (Harpp et al., 2014a).

1047

1048

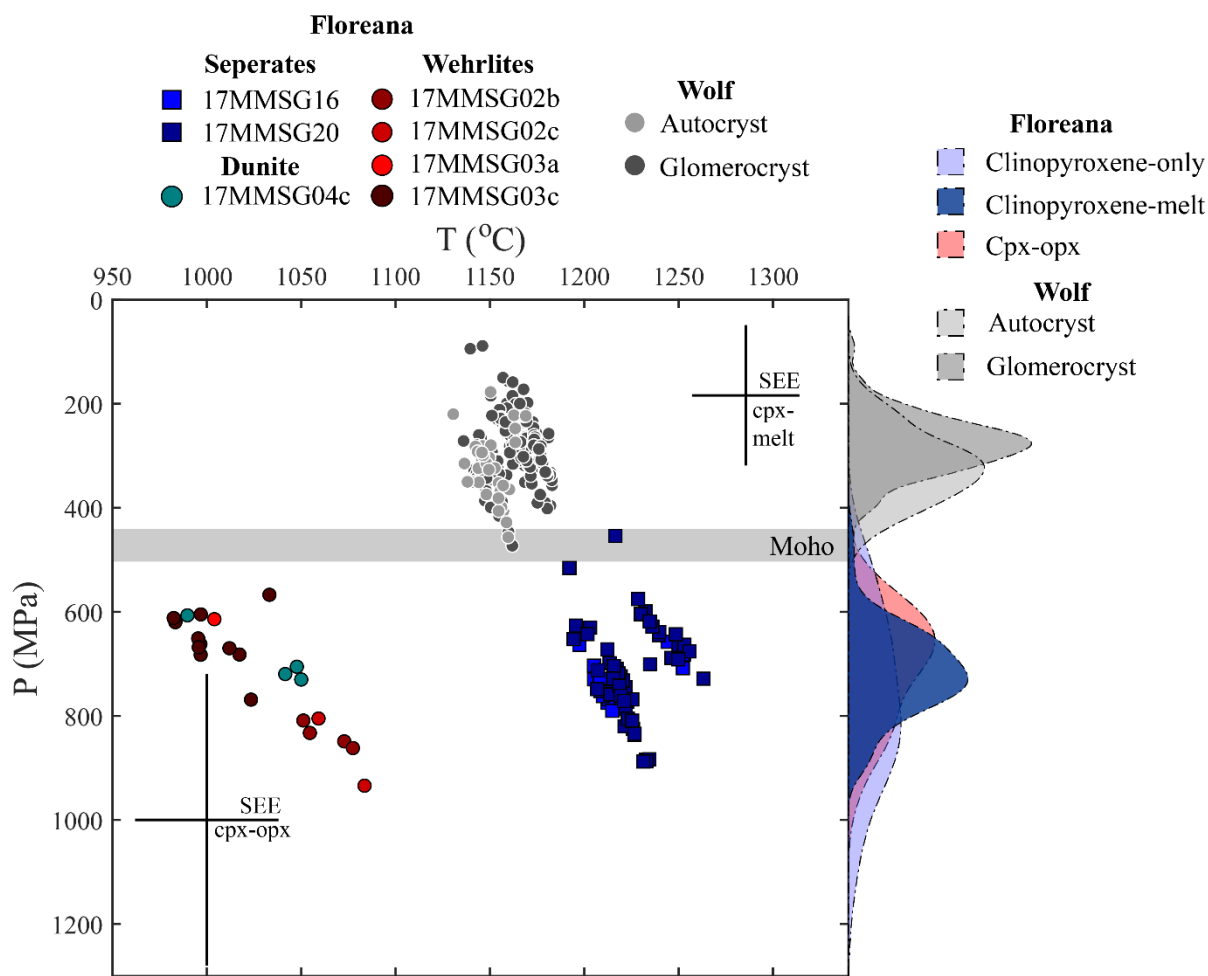
1049

1050

1051

1052

1053



1054

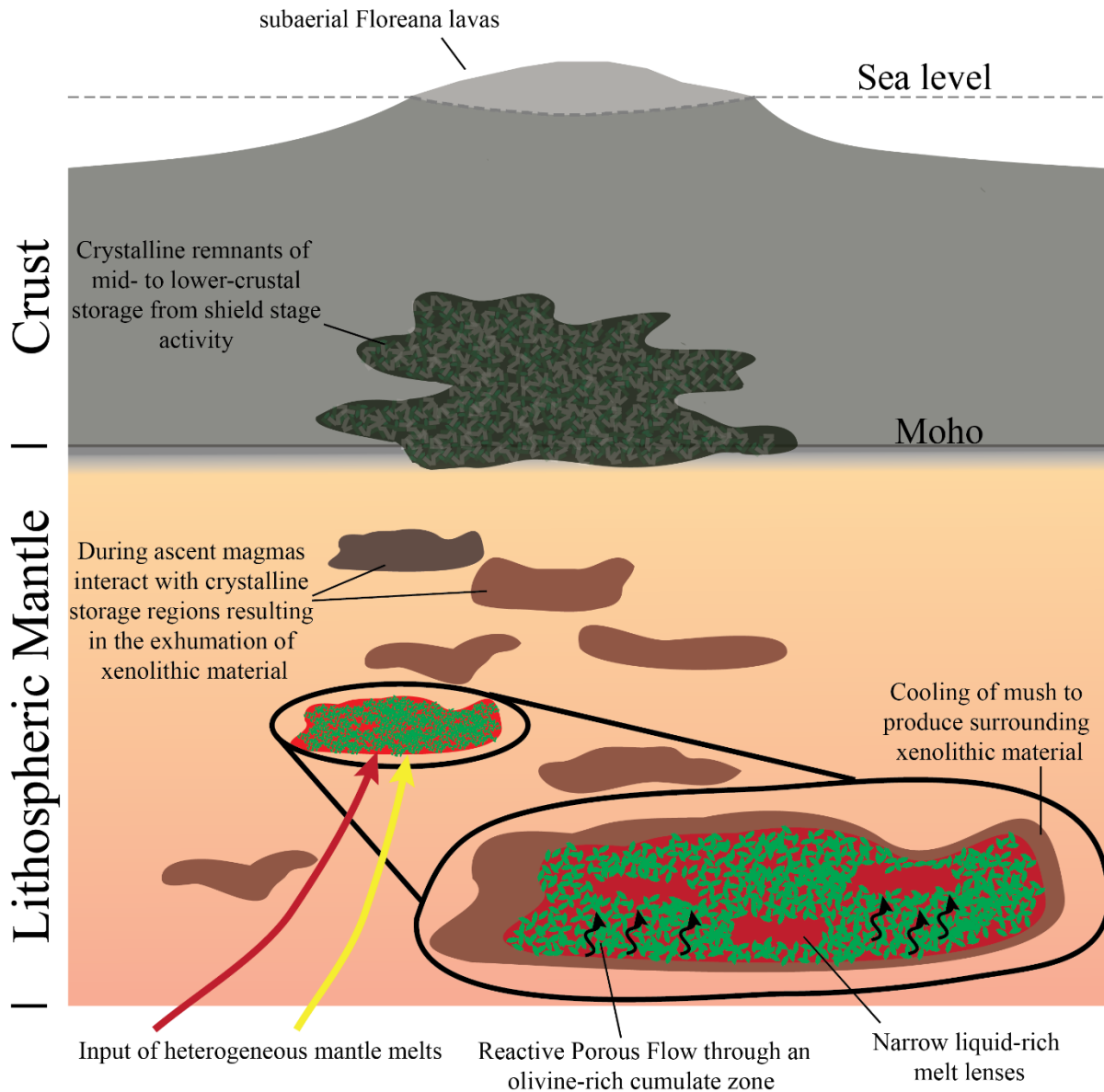
1055 **Figure 12** – Petrological thermobarometry results. The kernel density plots to the right show the
 1056 density distributions of barometric results from different models (light blue – clinopyroxene-only,
 1057 Putirka (2008); dark blue – clinopyroxene-melt, Neave and Putirka (2017); red – clinopyroxene-
 1058 orthopyroxene Putirka (2008)). The grey bar shows the Moho depth beneath Fernandina (from
 1059 Feighner and Richards, 1994) and the grey points and kernel density estimates show clinopyroxene-
 1060 melt thermobarometric results for autocrysts and glomerocrysts from Wolf volcano for comparison
 1061 (from Stock et al., 2018).

1062

1063

1064

1065



1066

1067

1068

1069

1070

1071

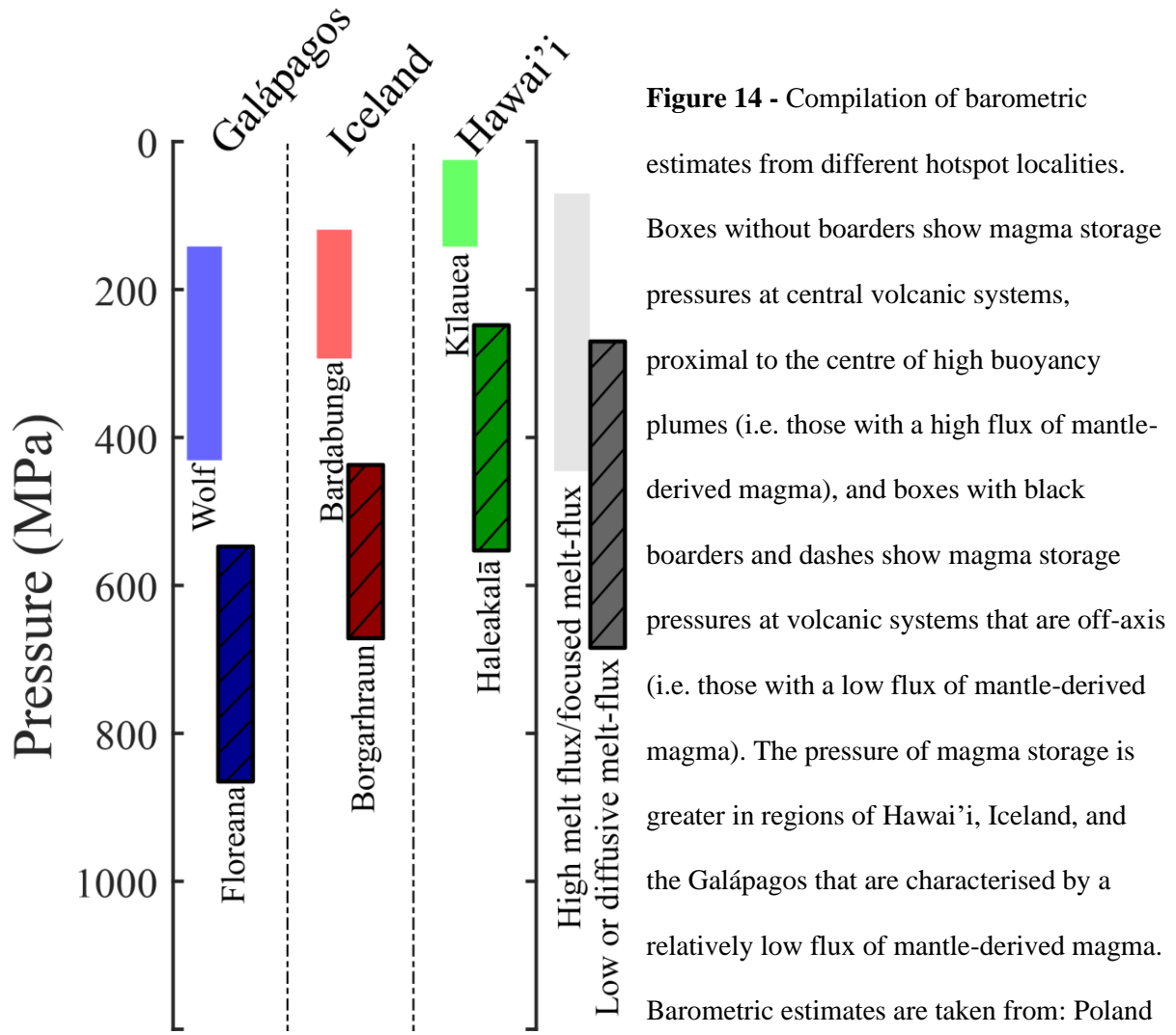
1072

1073

1074

1075

Figure 13 – Schematic illustration of the magma plumbing system beneath Floreana. No magma storage is identified within the crust. Instead, our barometric results indicate that Floreana magmas ascend directly from the upper mantle, where they are stored at a depth of $\sim 23.7 \pm 5.1$ km. Floreana magma storage regions are dominated by crystal-rich domains (i.e. mush). Reactive porous flow is identified as an important mechanism of melt migration and magma differentiation in the crystal-rich storage regions, although our results shows that some crystallisation occurs within liquid-rich domains.



1092 et al. (2015) for Kīlauea, using multiple available data streams to create a model of summit magma
 1093 storage (~25-150 MPa); Hammer et al. (2016) for Haleakalā using clinopyroxene melt barometry
 1094 (~400 ±160 MPa); Hartley et al. (2018) for Bardabunga using OPAM (210 ±70 MPa); Neave and
 1095 Putirka (2017) for Borgarhraun using clinopyroxene-melt barometry (570 ±120 MPa); Stock et al.
 1096 (2018) for Volcan Wolf using OPAM and clinopyroxene-melt barometry (280 ±140 MPa; OPAM
 1097 results), and this study for Floreana using clinopyroxene-melt barometry (717 ±165 MPa).